

Adjoint Sensitivity Analysis of High-Impact Extratropical Cyclones

JAMES D. DOYLE, CAROLYN A. REYNOLDS, AND CLARK AMERAULT

Naval Research Laboratory, Monterey, California

(Manuscript received 5 March 2019, in final form 3 July 2019)

ABSTRACT

The initial state sensitivity of high-impact extratropical cyclones over the North Atlantic and United Kingdom is investigated using an adjoint modeling system that includes moist processes. The adjoint analysis indicates that the 48-h forecast of precipitation and high winds associated with the extratropical cyclone “Desmond” was highly sensitive to mesoscale regions of moisture at the initial time. Mesoscale moisture and potential vorticity structures along the poleward edge of an atmospheric river at the initialization time had a large impact on the development of Desmond as demonstrated with precipitation, kinetic energy, and potential vorticity response functions. Adjoint-based optimal perturbations introduced into the initial state exhibit rapidly growing amplitudes through moist energetic processes over the 48-h forecast. The sensitivity manifests as an upshear-tilted structure positioned along the cold and warm fronts. Perturbations introduced into the nonlinear and tangent linear models quickly expand vertically and interact with potential vorticity anomalies in the mid- and upper levels. Analysis of adjoint sensitivity results for the winter 2013/14 show that the moisture sensitivity magnitude at the initial time is well correlated with the kinetic energy error at the 36-h forecast time, which supports the physical significance and importance of the mesoscale regions of high moisture sensitivities.


1. Introduction

Extratropical cyclones that form and intensify over the North Atlantic are well known for their large socioeconomic impacts downstream in the United Kingdom and Europe (e.g., [Enz et al. 2009](#); [Haylock 2011](#); [Pinto et al. 2012](#)). In the past several decades, a number of extratropical cyclones have occurred that had substantial impacts on the British Isles and Europe and generally have been poorly forecasted ([Ulbrich et al. 2001](#); [Wernli et al. 2002](#); [Walser et al. 2006](#); [Fink et al. 2009](#); [Liberato et al. 2013](#); [Doyle et al. 2014](#)). In spite of the remarkable advancements achieved in numerical weather prediction (NWP) (e.g., [Thorpe 2004](#); [Bauer et al. 2015](#)), the prediction of high-impact weather (i.e., strong winds and heavy precipitation) even on the short range is a formidable challenge, and the predictability barriers have yet to be fully identified (e.g., [Leutbecher et al. 2002](#); [Jung et al. 2004](#); [Hoskins and Coutinho 2005](#);

[Rodwell et al. 2013](#); [Frame et al. 2015](#)). Simulations of high-impact extratropical cyclones; for example, the October 1987 storm that impacted southern England ([Shutts 1990](#)), Lothar and Martin that impacted Europe ([Walser et al. 2006](#)), as well as U.S. East Coast snowstorms (e.g., [Langland et al. 2002](#); [Kleist and Morgan 2005a,b](#)) often exhibit strong initial state sensitivity.

In this study, we focus on an extratropical cyclone referred to as “Desmond” that impacted the United Kingdom, Ireland, Iceland, Norway, and Sweden in December 2015 with damaging winds and heavy precipitation that caused significant flooding. We then examine more broadly an especially active period over the North Atlantic and British Isles that featured a number of severe extratropical cyclones during the winter months of 2013/14.

The basic characteristics of extratropical cyclones are shaped by the jet stream and the associated meridional potential vorticity (PV) gradient (e.g., [Martius et al. 2010](#)). Incipient mesoscale disturbances that interact with the jet over the western Atlantic often evolve into synoptic-scale baroclinic systems with attendant cyclones and fronts ([Schwierz et al. 2004](#); [Schäfler et al. 2018](#)). For example, the European storm “Lothar” originated as a weak cyclone in the lower troposphere

 Denotes content that is immediately available upon publication as open access.

Corresponding author: James D. Doyle, james.doyle@nrlmry.navy.mil

DOI: 10.1175/MWR-D-19-0055.1

For information regarding reuse of this content and general copyright information, consult the [AMS Copyright Policy \(www.ametsoc.org/PUBSReuseLicenses\)](#).

that was associated with strong diabatic processes and a PV anomaly in the low levels (Wernli et al. 2002) and attained characteristics resembling a diabatic Rossby wave (e.g., Snyder and Lindzen 1991; Parker and Thorpe 1995). Diabatic processes influence the upper-tropospheric PV, as well as the characteristics of the baroclinic waves downstream (e.g., Massacand et al. 2001; Grams et al. 2011). An airstream known as a warm conveyor belt regulates diabatic processes in a cyclone through the vertical transport of warm and moist air that originates in the cyclone warm sector and ascends vertically (Browning et al. 1973; Harrold 1973; Browning 1990; Carlson 1980; Wernli and Davies 1997), and is strongly influenced by low-level moisture (Schäfler and Harnisch 2015). Diabatic heating within the warm conveyor belt leads to a low-level positive PV anomaly (Wernli and Davies 1997), which may feed back and influence the cyclone evolution (e.g., Davis et al. 1993; Binder et al. 2016). The role of diabatic processes within storm tracks has been a focus of the recent North Atlantic Waveguide and Downstream Impact Experiment (NAWDEX) (Schäfler et al. 2018).

Predictability and the concept of sensitivity are inherently interrelated. Sensitivity quantifies how a prediction is dependent on the initial state or the model itself. An ensemble forecast system that utilizes initial state perturbations and/or variations in the model formulation to represent forecast uncertainty can be used to compute the initial state or model sensitivity (e.g., Zhang et al. 2007; Torn and Hakim 2008; Torn and Hakim 2009; Durran et al. 2013). A limitation of ensemble forecast sensitivity is that the full distribution of potential forecasts states should be represented, requiring a large number of ensemble members with significant computational expense, particularly for applications at high resolution.

An alternative approach to efficiently calculate sensitivity uses an adjoint [for an overview see Errico (1997)]. Adjoint and singular vector methods have been used to diagnose the sensitivity and predictability characteristics of many meteorological phenomena including: extratropical cyclones (Gelaro et al. 1998; Langland et al. 2002; Coutinho et al. 2004; Hoskins and Coutinho 2005; Doyle et al. 2014), synoptic- and large-scale dynamics (Reynolds and Gelaro 2001; Reynolds et al. 2001; Kleist and Morgan 2005a), atmospheric rivers (Reynolds et al. 2019), tropical cyclones (Hoover and Morgan 2011), adjustment processes (Morgan 2018), and observing system design and targeting (Gelaro et al. 1999; Langland et al. 1999; Szunyogh et al. 2000; Leutbecher et al. 2002; Majumdar 2016). In this study, results from a mesoscale adjoint model and associated adjoint-based optimal perturbations (discussed in section 2c)

are analyzed to explore the degree to which initial state sensitivity influences the predictability of high-impact North Atlantic extratropical cyclones.

The sensitivity of extratropical cyclones to the model initial state and the limits of predictability have been considered by a number of studies. The “surprise” snowstorm of January 2000 on the U.S. East Coast was noteworthy because of the high impact and poor performance of the operational numerical weather predictions. Adjoint sensitivity calculations identified regions of high sensitivity over the eastern Pacific that were coincident with analysis uncertainty (Langland et al. 2002), a result that was confirmed through analysis of ensemble forecasts (e.g., Zhang et al. 2002; Zhang et al. 2003). Initial state sensitivities were found to be maximized along a baroclinic zone with an upshear vertical tilt (Kleist and Morgan 2005a). Other cases of extratropical cyclones and storm tracks note that rapidly growing structures or singular vectors (SVs) (Molteni and Palmer 1993; Buizza and Palmer 1995) tend to be tilted vertically against the wind shear and collocated with PV anomalies (Reynolds et al. 2001). Rapid perturbation growth ensues initially with the “unshielding” of smaller-scale PV structures (Orr 1907; Farrell 1982; Badger and Hoskins 2001) due to the vertical wind shear (e.g., Errico and Vukicevic 1992; Reynolds et al. 2001). It should be noted that perturbation growth rates are sensitive to the horizontal resolution (Ancell and Mass 2006, 2008).

Increased perturbation and error growth has been found to occur in moist simulations (Tan et al. 2004; Hoskins and Coutinho 2005). The ensemble-based study of Zhang et al. (2007) hypothesized that the error growth is initially dominated by convective instabilities on the smaller scales, which then traverse upscale energetically to contaminate the synoptic scales. However, the growth of medium- to larger-scale perturbations were found by Durran et al. (2013) to be the most important for two cases of cyclogenesis.

The objective of this study is to build on the previous research of Doyle et al. (2014) to further explore the forecast sensitivity of North Atlantic baroclinic waves to the initial conditions and to identify key predictability barriers for these high-impact cyclones. We focus especially on the forecast sensitivity associated with the initial state humidity because recent research has pointed to the importance of enhanced moisture sensitivity on forecast evolution (e.g., Doyle et al. 2014; Reynolds et al. 2019), and the difficulty of observing and analyzing moisture, particularly over the ocean basins. In this study, we highlight some of the key similarities and differences found in these investigations. The formulations of the nonhydrostatic model, as well as the tangent

linear and nonlinear models are summarized briefly in [section 2](#). An analysis of the sensitivity results for extratropical cyclone Desmond in 2015 is presented in [section 3](#). [Section 4](#) contains the adjoint sensitivity results for the winter of 2013/14. The summary and conclusions can be found in [section 5](#).

2. Nonlinear and adjoint numerical model description

The description of the nonlinear, tangent linear, and adjoint modeling system is drawn from the model background described in [Doyle et al. \(2012, 2014\)](#).

a. Nonlinear numerical model

The atmospheric portion of the Coupled Ocean–Atmosphere Mesoscale Prediction System (COAMPS; [Hodur 1997](#); [Doyle et al. 2012, 2014](#)) is used in this study. COAMPS is based on the compressible, nonhydrostatic equations and uses a semi-implicit numerical method following [Klemp and Wilhelmson \(1978\)](#). The finite differences are of second-order accuracy and fourth-order accurate horizontal diffusion is used. A horizontally staggered C grid and a vertically staggered terrain-following height coordinate are used.

The model predicted variables include the wind components, u , v , and w , potential temperature, perturbation pressure, water vapor (mixing ratio), water and ice microphysical species, and turbulent kinetic energy (TKE). The cloud microphysical processes are parameterized using a modified [Rutledge and Hobbs \(1983\)](#) methodology. A moisture convergence closure is used for the deep convection parameterization ([Molinari 1985](#)). The TKE budget is used to parameterize turbulent mixing and diffusion processes in the boundary layer and free atmosphere, along with parameterized surface fluxes ([Louis 1979](#)) and a slab force-restore model used for the surface energy budget over land. The nonlinear, adjoint, and tangent linear models use physical parameterizations that are identical in their formulations. Radiative processes in the tangent linear and adjoint models are not included due to the complexities with nonlinearities in the physics (e.g., [Zou et al. 1993](#); [Vukicevic and Errico 1993](#); [Holdaway et al. 2014](#)). The adjoint and tangent linear models make use of ice-phase microphysics, in contrast to the [Doyle et al. \(2012 and 2014\)](#) studies that neglected ice microphysics.

The nonlinear, adjoint and tangent linear models use a horizontal grid increment of 36 km with 221×131 grid points for the storm Desmond simulations, and a 45 km resolution for the winter 2013/14 simulations with 201×161 points. The number of vertical levels for all

simulations is 45. A sponge is applied over a 10-km layer at the model top to minimize gravity wave reflections. The model top in these simulations is located at 30 km. The terrain digital elevation model is used following [Doyle et al. \(2012\)](#). The initial conditions are created from the NOAA Global Forecast System (GFS) operational analyses and the lateral boundary conditions are derived from GFS forecasts.

b. Adjoint and tangent linear models

An adjoint allows for the quantitative computation of sensitivity of a forecast metric or response function to changes in the initial state (e.g., [Errico 1997](#)). The impact of the initial state (\mathbf{x}_{t_0}) on a forecast metric, J (model state \mathbf{x}_t at time t) can be expressed as

$$J(\mathbf{x}_t) = J[M(\mathbf{x}_{t_0})], \quad (1)$$

where M is the nonlinear forecast model and J can be interpreted as a response function (background discussion closely follows that of [Doyle et al. 2012, 2014](#)). In data assimilation applications, J is often referred to as the cost function. The relationship between the initial and forecast states can be found through the gradient of the metric J with respect to the initial model state:

$$\frac{\partial J}{\partial \mathbf{x}_{t_0}} = \mathbf{M}^T \frac{\partial J}{\partial \mathbf{x}_t}, \quad (2)$$

where \mathbf{M} is the tangent linear model constructed about the trajectory from the nonlinear model M and the superscript T denotes the transpose operation with \mathbf{M}^T yielding the adjoint model. It follows that the adjoint forcing can be computed as $\partial J / \partial \mathbf{x}_t$, given a continuous and differentiable response function. As an example, if J is selected as the integrated kinetic energy in a box, the sensitivity of the forecast kinetic energy at 48 h (with $\mathbf{x}_t = 48$ h) to the initial state (at $\mathbf{x}_{t_0} = 0$ h) can be computed following (2) using the adjoint model, \mathbf{M}^T .

The description of the tangent linear and adjoint COAMPS models ([Amerault et al. 2008](#); [Doyle et al. 2012](#)) closely follows that of [Doyle et al. \(2012, 2014\)](#) with some modifications. The tangent linear and adjoint models include the nonhydrostatic dynamical core, as well as parameterizations for the TKE, surface layer, force restore soil, cumulus, and explicit moist physics processes. Vertical diffusion terms are not considered in the adjoint and tangent linear models (e.g., [Mahfouf 1999](#)). The nonlinear model trajectory is saved every time step (45 s for the simulations discussed), which is important when applying the tangent linear and adjoint models with moist processes and microphysics. The

horizontal resolution utilized in this study, 45- and 36-km grid increments, is generally comparable to or higher resolution than used in other adjoint-based studies.

c. Adjoint-based optimal perturbations

Adjoint-based optimal perturbations are derived following the methodology of Errico and Raeder (1999), Rabier et al. (1996) and Oortwijn and Barkmeijer (1995) and subsequently evolved using the tangent linear and nonlinear models. Additional details of the methodology described below can be found in Doyle et al. (2012 and 2014). Perturbations (following Doyle et al. 2012) to a scalar metric or response function J of the forecast can be expressed as

$$J' = \sum_j \frac{\partial J}{\partial x_j} x'_j, \quad (3)$$

where $\partial J/\partial x_j$ is the adjoint gradient of the response function with respect to the j th component of the initial state. The \mathbf{x} and \mathbf{x}' components are valid at time t_0 in Eqs. (3)–(6), and it should be noted that for clarity purposes the subscript is not shown. The perturbation vector \mathbf{x}' (j th component) is optimal for weights w_j following

$$x'_j = \frac{s}{w_j} \frac{\partial J}{\partial x_j}. \quad (4)$$

The constraint I ,

$$I = \sum_j w_j x_j'^2, \quad (5)$$

is imposed to solve (4), with the scaling parameter s ,

$$s = \sqrt{2I} \left[\sum_j \frac{1}{w_j} \left(\frac{\partial J}{\partial x_j} \right)^2 \right]^{-1/2}. \quad (6)$$

The weights w_j are based on the largest forecast differences of the state components for each variable on each vertical level using the methodology following Doyle et al. (2012 and 2014). The scaling s (units of J^{-1}) in Eq. (4), is based on the *largest* perturbation of either the u component of the wind speed, potential temperature, or water vapor, such that the perturbation does not exceed 1 m s^{-1} , 1 K , or 1 g kg^{-1} , respectively. These magnitudes are comparable to the prescribed radiosonde and dropsonde observation errors in the COAMPS data assimilation system. All of the prognostic variables are perturbed with the exception of the TKE and the microphysical species.

d. Response functions

One of the objectives of this study is to explore the impact of the response function choice on the sensitivity calculations. Total energy or kinetic energy (KE) response functions are predominantly used in adjoint and singular vector studies, although occasionally other norms have been used. These include precipitation (Errico et al. 2003; Mahfouf and Bilodeau 2007; Zhou and Cui 2015; Reynolds et al. 2019) and convective available potential energy (Stappers and Barkmeijer 2011) response functions. High-impact extratropical cyclones considered in this study are often associated with high winds and intense precipitation, and it follows that we consider KE, precipitation, as well as PV response functions.

Simulations for the storm Desmond are performed with the following response functions: (i) KE defined as $1/2(u^2 + v^2 + w^2)$, (ii) accumulated precipitation, (iii) integrated rain and snow concentration, and (iv) PV. The response functions are computed over a $504 \times 504 \text{ km}^2$ box (15×15 grid points on the 36-km resolution mesh). The response function for the Desmond simulations is centered over the northern portion of England where the heaviest precipitation and high wind speeds occurred with the exception of the PV response function, which was centered to the west of Ireland near a strong PV filament forecasted at the 48-h time. The KE response function extends vertically over the lowest 860 m (11 model layers) of the model. The two precipitation response functions are applied only at the lowest model level for the integrated rain and snow concentration and at the surface for the accumulated precipitation response function. The J in Eq. (2) for the accumulated precipitation can be specified for any arbitrary length in the forecast. For example, if J is the accumulated precipitation between the final time t_f and a time during the forecast t_1 , the gradient of J can be expressed as

$$\frac{\partial J}{\partial \mathbf{x}_{t_0}} = \mathbf{M}^T \left[\frac{\partial J}{\partial \mathbf{x}_{t_f}} - \frac{\partial J}{\partial \mathbf{x}_{t_1}} \right]. \quad (7)$$

In contrast to other metrics like KE or PV, which are assessed at the final forecast time, the sensitivity using the accumulated precipitation metric corresponds to the entire period over which the accumulated precipitation has been selected. For the Desmond case, the accumulated precipitation response function is computed over the 24-h period between 0000 UTC 5 December and 0000 UTC 6 December. The integrated rain and snow concentration is computed for the same 24-h period computing the response function every 3 h. The PV response function is applied in the vertical between 540 and 2300 m, which spans the region of a low-level PV

maximum. The initialization time for the Desmond simulation is 0000 UTC 4 December and a 48-h simulation is conducted with identical length adjoint and tangent linear integrations.

For the North Atlantic simulations, the response functions are computed over a box that extends horizontally over a $630 \times 630 \text{ km}^2$ region (15×15 grid points on the 45-km resolution mesh). For these simulations, only the (i) KE and (ii) accumulated precipitation are considered. The response function for the North Atlantic simulations is centered over the British Isles. The vertical extent of the KE response function is once again in the lowest 860 m (11 model layers) and the accumulated precipitation response function is applied at the surface over the 24–36-h forecast time period. The North Atlantic adjoint calculations are 36 h in length and performed every 6 h for the period of 1 December 2013–28 February 2014.

e. Adjoint accuracy

The COAMPS tangent linear and adjoint models satisfy the standard tests for correctness of the adjoint (e.g., gradient and perturbation tests) following Amerault et al. (2008). The adjoint results are predominantly insensitive to the horizontal and vertical dimensions of the response function region. The accuracy of the tangent linear model is routinely assessed through comparison of the nonlinear and tangent linear forecasts evolved with optimal perturbations introduced in the initial states. The correlation between the tangent linear and nonlinear evolved perturbations generally varies between 0.5 and 0.8 for the zonal wind component, temperature, water vapor, kinetic energy, and precipitation which indicates that the tangent linear approximation is valid (e.g., see Doyle et al. 2014). For example, the correlation between the tangent linear and nonlinear evolved perturbations for a 48-h integration for the Desmond case using a kinetic energy response function is: 0.6 for zonal wind, 0.6 for temperature, 0.5 for water vapor, 0.5 for precipitation, and 0.5 for kinetic energy. The correlation for a similar experiment using a precipitation response function is 0.8 for zonal wind, 0.7 for temperature, 0.8 for water vapor, 0.8 for precipitation, and 0.7 for kinetic energy. The relatively high correlation between the evolved perturbations in the tangent linear and nonlinear models demonstrates the utility of the adjoint model results for both the Desmond and North Atlantic simulations for their respective integration periods.

3. Storm Desmond

In this section, an overview is provided of the meteorological conditions associated with the development

of Desmond, followed by an analysis of the adjoint sensitivity results for this storm. Additionally, we quantify the impact of the choice of response function on the sensitivity, along with an analysis of the energetics of the optimal perturbations.

a. Synoptic-scale description

The extratropical cyclone Desmond greatly impacted the British Isles during 4–6 December 2015 through exceptionally strong winds with gusts up to 40 m s^{-1} in the United Kingdom and record amounts of precipitation for the United Kingdom of 341 mm over 24 h and 405 mm over 48 h in northwest England (McCarthy et al. 2016; Matthews et al. 2018). The hydrological impacts of Desmond were severe, with a number of U.K. and Irish rivers recording all-time peak discharge records (Matthews et al. 2018). The overall damage costs in the United Kingdom were estimated at \$500–\$650 million [U.S. dollars (USD); PwC 2015, PwC; https://pwc.blogs.com/press_room/2015/12/updated-estimates-on-cost-of-storm-desmond-pwc.html]. Additionally, Desmond also caused further damage in Scandinavia including numerous landslides in Norway (Dijkstra et al. 2016). The operational forecasts failed to capture the extreme precipitation amounts, flash floods, and high winds, although ensemble products such as the European Centre for Medium-Range Weather Forecasts (ECMWF) extreme forecast index showed considerable utility (Lavers et al. 2016).

The NOAA GFS analysis at 0000 UTC 5 December 2015 (Fig. 1a) shows a deep surface cyclone with a central pressure of 940 hPa near Iceland positioned beneath an upper-level PV anomaly. The cyclone featured a trailing cold front with a stationary front extending southwestward to the north-central Atlantic with a developing frontal wave associated with a PV anomaly aloft. The infrared satellite imagery (Fig. 1b) indicates extensive cloud cover from Scandinavia to the British Isles and extending westward along the stationary front. The satellite-based precipitable water valid at 0000 UTC 5 December (Fig. 1c) indicates an extensive moist plume or atmospheric river (AR) feature extending northeastward from the subtropical western Atlantic to Ireland. ARs account for over 90% of the horizontal water vapor transport in the midlatitudes (Zhu and Newell 1998) and are often associated heavy precipitation and coastal flooding (Ralph et al. 2004, 2011, 2018; Lavers et al. 2011; Neiman et al. 2008; Lavers and Villarini 2013). Accurate numerical weather prediction forecasts of atmospheric rivers can be challenging. For example, Lavers et al. (2018) used reconnaissance dropsondes assimilated into the ECMWF Integrated Forecasting System and found short-range forecast errors of water vapor fluxes to be $\sim 22\%$ of the mean observed flux.

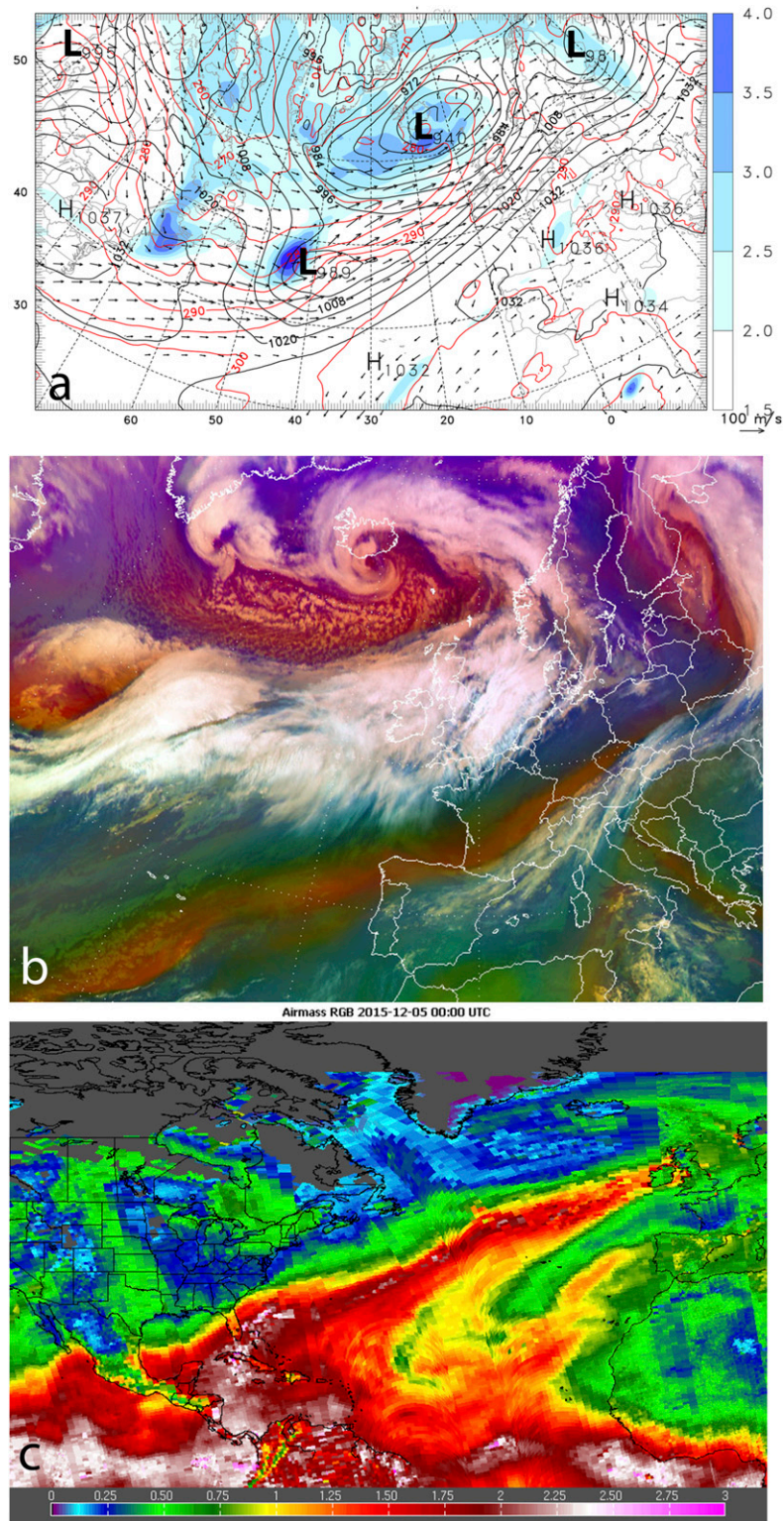


FIG. 1. (a) The NOAA GFS analysis is shown valid at 0000 UTC 5 Dec. Displayed are the 330 K potential vorticity (PVU or $\text{K m}^2 \text{kg}^{-1} \text{s}^{-1}$ blue shading), wind vectors (every 6 grid points, winds greater than 20 m s^{-2} shown) on the 330 K surface, 850-hPa potential temperature (red isotherms every 5 K), and sea level pressure (black isobars every 6 hPa). Satellite imagery valid at 0000 UTC 5 Dec 2015 from (b) *Meteosat-10*

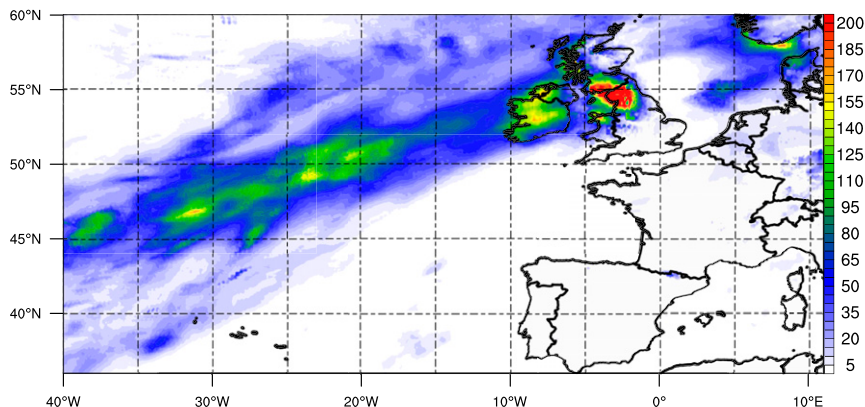


FIG. 2. Accumulated precipitation (mm) from NASA Integrated Multisatellite Retrievals for GPM (IMERG) dataset valid for 0000 UTC 4 Dec–0000 UTC 6 Dec.

The accumulated precipitation (mm) from the NASA Integrated Multisatellite Retrievals for GPM (IMERG) dataset valid for 0000 UTC 4 December–0000 UTC 6 December is shown in Fig. 2. The extreme precipitation over northwest England, southern Scotland, and Ireland is apparent, with a broad maximum of over 180 mm over the 48-h period.

b. Adjoint sensitivity results using a kinetic energy response function

The adjoint and tangent linear models are applied to investigate the initial condition sensitivity for Desmond using an initialization time of 0000 UTC 4 December and an integration time period of 48 h. The sensitivity of the 48-h KE in the response function box (magenta rectangle) in the lowest 860 m to the initial state water vapor (mixing ratio) is presented in Fig. 3. Positive (negative) sensitivity implies that an increase in water vapor will increase (decrease) the strength of the winds in the response function region at the 48-h forecast time. The incipient surface cyclone associated with storm Desmond is apparent in Fig. 3a at 0000 UTC 4 December with the sea level pressure minimum located near 55°N and 30°W. The 850- and 700-hPa water vapor sensitivity (Figs. 3a,c) indicate sensitivity maxima and minima located along the northwestern flank of the AR to the east of the northeastern U.S. and eastern Canadian coasts, coincident with a short-wave trough southwest of the Greenland tip (geopotential height shown in Figs. 3b and 3d). The potential temperature sensitivity (not shown) has a similar structure. The results suggest

that warming and moistening within the relatively small-scale regions of high sensitivity at the initial time results in an increase of the winds and KE at the 48-h time. It should be noted that only a relatively small portion of the AR at the initial time (Figs. 3a,c) is key for the intensification of Desmond and the high-impact winds.

The u - and v -wind component sensitivity (not shown) indicates maxima and minima associated with both short-wave troughs. The northern short-wave trough leads to the intensification of the deep surface cyclone south of Iceland (Fig. 1a) and the trough axis becomes meridionally aligned by the 48-h time embedded in strong southwesterly flow over the British Isles. The PV perturbation field (Figs. 3b,d) is computed to elucidate the mesoscale and synoptic-scale dynamics based on the nonlinear model trajectory and adjoint optimal perturbations (hereafter referred to as the PV perturbations):

$$PV' = \left[\frac{1}{(\rho + \rho')} (\zeta'_a + \zeta'_a) \cdot \nabla(\theta + \theta') \right] - \left[\frac{1}{\rho} \zeta'_a \cdot \nabla\theta \right],$$

where ρ is the density, θ is the potential temperature, and ζ'_a is the vertical component of the absolute vorticity, with prime variables corresponding to the adjoint optimal perturbations. Vorticity computed from optimal perturbations of zonal and meridional winds projects onto the sensitivity with respect to vorticity, however the sensitivity with respect to vorticity is broader in scale as the magnitude is proportional to the inverse Laplacian of the vertical component of the curl of the sensitivity to the wind components (Kleist and Morgan 2005b).

←

RGB infrared image (from EUMETSAT) and (c) precipitable water (in.) valid at 0000 UTC (from Cooperative Institute for Research in the Atmosphere–Colorado State University).

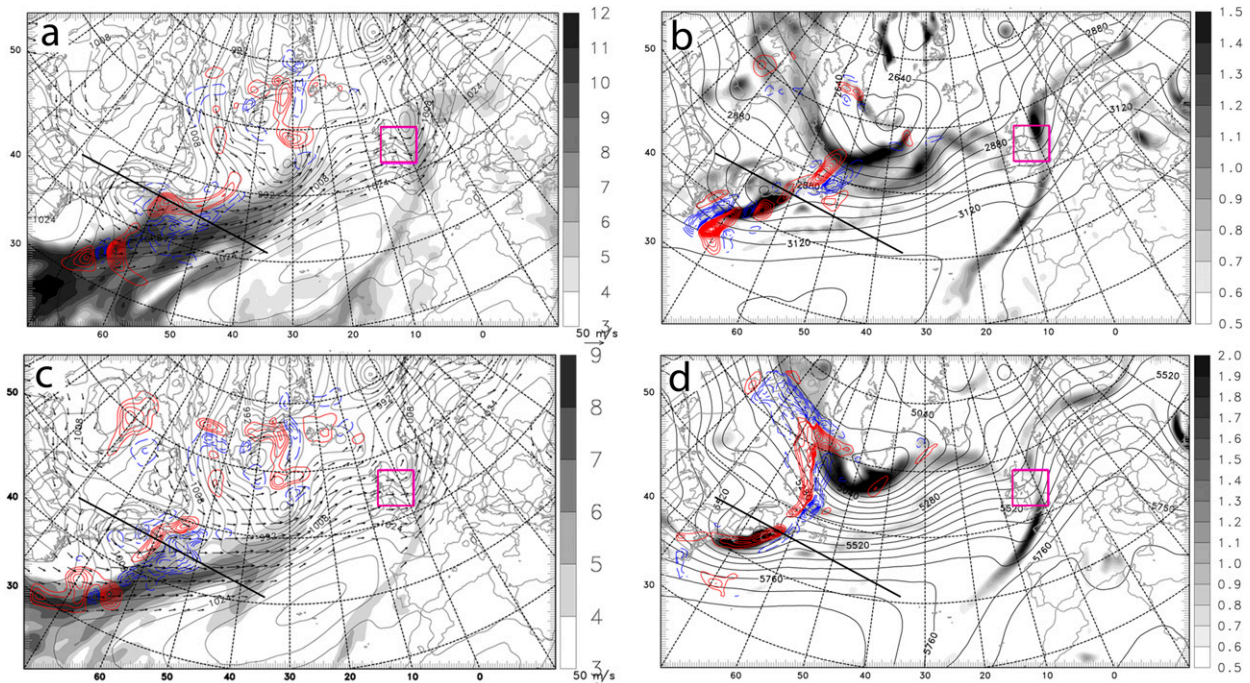


FIG. 3. Horizontal plan views of the initial condition and sensitivity fields valid at 0000 UTC 4 Dec 2015 using the kinetic energy response function (location shown by the magenta box). (a) 850-hPa water vapor (g kg^{-1} in gray shading intervals every 1 g kg^{-1}), 850-hPa water vapor sensitivity [positive (red) and negative (blue) contours with an interval of $0.03 \text{ m}^2 \text{ s}^{-2} (\text{g kg}^{-1})^{-1}$], sea level pressure (black isobars every 4 hPa), and 850-hPa wind vectors greater than 15 m s^{-1} (every sixth grid point), (b) 700-hPa potential vorticity (PVU in gray shading intervals every 0.1 PVU), 700-hPa geopotential every 60 m (black contours), and the 700-hPa PV perturbations [positive (red) and negative (blue) contours with interval every 0.01 PVU], (c) as in (a), but for 700 hPa, (d) as in (b), but for 500 hPa. The sensitivities in (a) and (c) are scaled by $10^5 \text{ km}^3/(\Delta x \Delta y \Delta z)$. The solid bold black line indicates the location of the cross section in Fig. 4.

Similarly, the sensitivity to the PV is likely broader than the PV computed from the optimal perturbation (Hoover, personal communications). Nevertheless, the PV perturbations project on to the PV sensitivity and indicate the regions of high sensitivity involving the PV. Computation of PV sensitivity remains a challenge for complex numerical weather prediction models (e.g., Morgan 2018).

The PV perturbation field at 700 hPa (Fig. 3b) indicates an elongated maximum near the northwestern flank of the AR and near the short-wave trough east of the Canadian coast. At 500-hPa, the optimal perturbations are greatest just upstream of the closed low at the southern tip of Greenland. Enhancements to the elongated PV anomaly will lead to an intensification of the low-level winds at the 48-h time. The negative PV perturbation regions located adjacent to regions of positive PV perturbations (e.g., near 50°N , 50°W) imply that a shift in the PV anomaly will lead to an increase in KE in the response function region. The initial-time mid-tropospheric wind and temperature sensitivity are approximately 2 times greater than the sensitivity near the tropopause. However, the optimal perturbations grow quickly in magnitude and become more vertically

extensive by the 24-h forecast time (similar to the results in Reynolds et al. 2001). The perturbations then modulate the upper-tropospheric PV and steepen the tropopause within the early part of the forecast through the growth of these initial perturbations that are maximized in the low to midtroposphere.

The moisture sensitivity [$\text{g kg}^{-1} (\text{m}^2 \text{ s}^{-2})^{-1}$] has maximum magnitudes approximately 5–10 times that of the horizontal wind sensitivity [$\text{m s}^{-1} (\text{m}^2 \text{ s}^{-2})^{-1}$] and 1.5 times that of the potential temperature sensitivity [$\text{K} (\text{m}^2 \text{ s}^{-2})^{-1}$], similar to that found by Doyle et al. (2014) and Reynolds et al. (2019). Using approximate values of observational uncertainty to scale the sensitivity, as applied in the COAMPS data assimilation system, namely $1\text{--}1.5 \text{ g kg}^{-1}$, 1.8 m s^{-1} , and 1 K , for the moisture, winds, and temperature, respectively, the moisture sensitivity is the largest followed by the temperature sensitivity. The importance of the moisture sensitivity is not surprising given the key role of latent heat release during cyclogenesis (e.g., Kuo et al. 1991; Wernli et al. 2002).

Vertical cross sections of the water vapor sensitivity and PV perturbation fields are shown in Figs. 4a and 4b, respectively. The vertical cross section location denoted

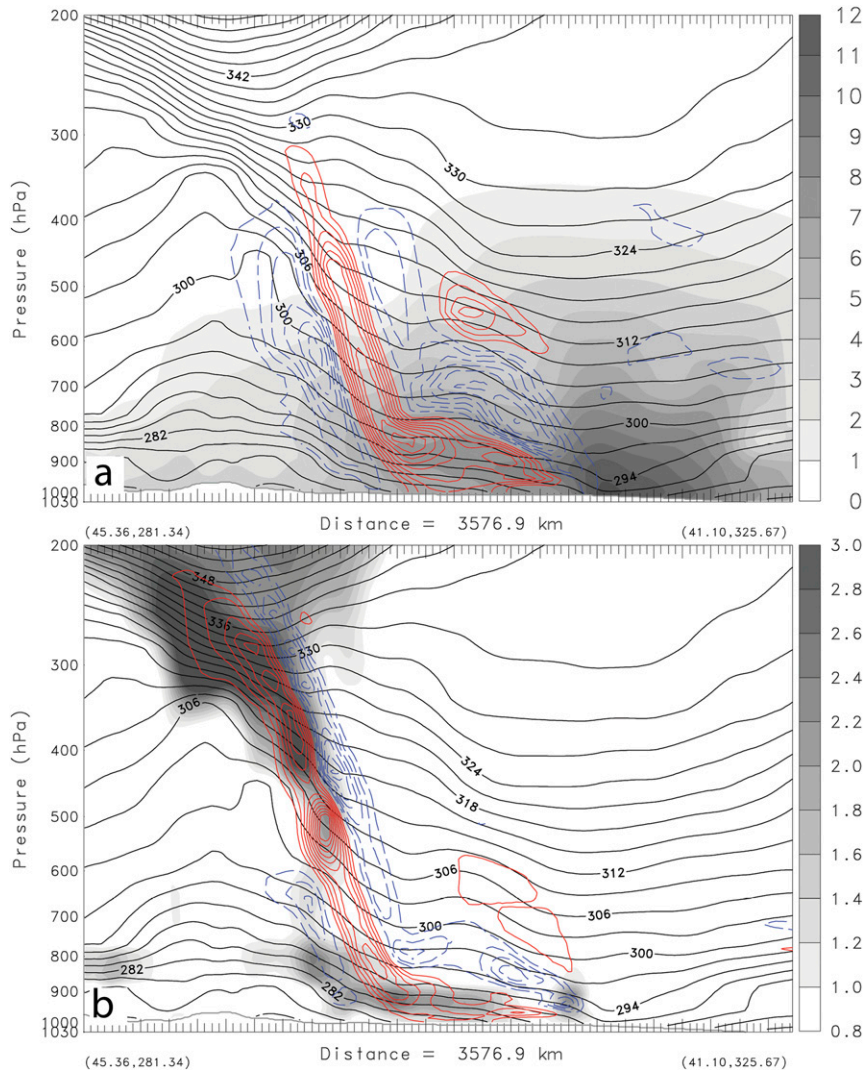


FIG. 4. Vertical cross section oriented northwest to southeast (location shown in Fig. 3) of the initial condition and sensitivity fields valid at 0000 UTC 4 Dec 2015 using the kinetic energy response function. (a) Water vapor (g kg^{-1} in gray shading intervals every 1 g kg^{-1}), isentropes are shown with the black contours (every 3 K), water vapor sensitivity [positive (red) and negative (blue) contours with an interval of $0.02 \text{ m}^2 \text{ s}^{-2} (\text{g kg}^{-1})^{-1}$], (b) potential vorticity (PVU in gray shading intervals every 0.2 PVU), isentropes are shown with the black contours (every 3 K), and the PV perturbations [positive (red) and negative (blue) contours with interval every 0.005 PVU]. The sensitivities in (a) are scaled by $10^5 \text{ km}^3 / (\Delta x \Delta x \Delta z)$.

by the thick black lines in Fig. 3 is approximately normal to the sensitivity features as well as the frontal zone at low and midlevels. The water vapor sensitivity maximum slopes along the front, with a secondary maximum near the 900-hPa level. The sensitivity is strongest in elongated structures along the cold and warm frontal zones as evident in Figs. 3a and 3c. The negative water vapor sensitivities that flank the sloping positive sensitivity suggests that a sharpening of the moist frontal ascent will lead to a stronger short wave and wind speeds (KE) in the forecast. Additionally, reducing the mixing ratio

in these negative sensitivity regions will lead to a strengthening of the winds at the 48-h forecast time through an increase of the pressure and thermal gradients along the front, which in turn reinforce the latent heating. The forecast of the strong winds associated with Desmond is primarily sensitive to initial-state changes in the lower and midtroposphere along both the cold and warm fronts (Figs. 3a,c). The moisture sensitivity along the warm front is less defined in this incipient cyclone in contrast to the Xynthia case, which had a well-developed warm conveyor belt at the initial time (Doyle et al. 2014).

The PV perturbations (Fig. 4b) show a narrow sloping maximum along the front similar to the structure of the water vapor sensitivity. These banded PV perturbation structures are positioned beneath a very strong upper-level jet ($>85 \text{ m s}^{-1}$ at 300 hPa) in a region of strong vertical wind shear, exhibiting similarities to studies utilizing singular vectors (e.g., Reynolds et al. 2001). The PV perturbations for this incipient cyclone suggest that enhancing the PV along the front, sharpening the PV gradient, and extending it to lower altitudes (Fig. 4b) will enhance the 48-h forecast low-level winds, similar to the results found by Doyle et al. (2014) for a more mature extratropical cyclone. These results are in broad agreement with more theoretically based studies of Badger and Hoskins (2001) and Morgan (2001) that emphasize the important interactions between PV and surface-based thermal anomalies for rapidly growing perturbations.

The nonlinear model forecast and the corresponding evolved optimal perturbations based on the KE response function sensitivity are analyzed for this simulation. At the 48-h simulation time (0000 UTC 6 December), a strong low-level jet is positioned over northern England and southern Scotland with a 500-m wind speed maxima in excess of 25 m s^{-1} (Fig. 5a). The evolved optimal perturbations result in an increase of 500-m wind speeds by more than 10 m s^{-1} in the northeastern portion of the response function region (Fig. 5b). The strengthening of the low-level jet arises from a deepening of the frontal wave along the northern portion of the British Isles and high pressures to the southwest, both of which increase the pressure gradient over the response function region. The 48-h accumulated precipitation valid at 0000 UTC 6 December is shown in Fig. 6a. The largest precipitation maxima are located over Ireland and the northwestern portion of Scotland and the model fails to capture the heavy precipitation in northwestern England as observed (Fig. 2). The optimal perturbation impact on the accumulated precipitation (perturbation shown in Fig. 6b) indicates a banded region of increased precipitation outside the response function box near the frontal wave, which is reasonable given that the RF used in this simulation is KE and is not optimized for accumulated precipitation.

c. Adjoint sensitivity results using precipitation and potential vorticity response functions

A series of adjoint simulations are carried out with other response function options to provide further insight into how the metric influences the sensitivity. Additional simulations for the storm Desmond are performed with response functions for the accumulated precipitation and PV. The precipitation response function is specified over a 24-h period from 0000 UTC

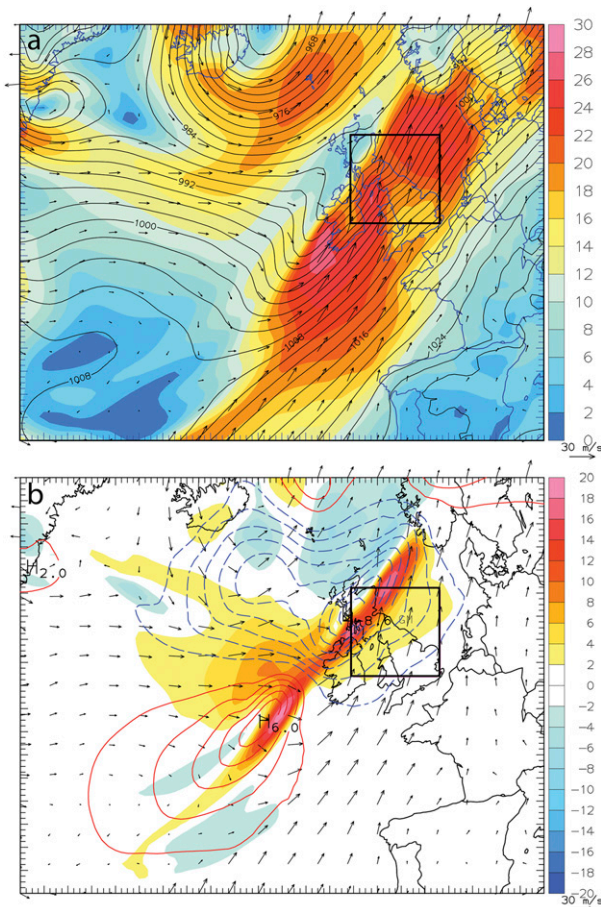


FIG. 5. Horizontal plan view shown for a subdomain region at the 48-h simulation time valid at 0000 UTC 6 Dec 2015 for the (a) wind speed at 500 m (color fill every 2 m s^{-1}), sea level pressure (every 2 hPa), and wind vectors at 500 m (every fifth grid point), and (b) optimal perturbation wind speed at 500 m (color fill every 2 m s^{-1}), 500-m total wind vectors, and optimal perturbation pressure at 500 m [positive (red) and negative (blue) contours every 1 hPa]. The response function region is shown by the black box.

5 December to 0000 UTC 6 December. The sensitivity results for the response function using the 24-h accumulated precipitation are very similar to a response function using the rainwater and snow concentrations in the lowest model level averaged over the same 24-h period using a 3-h interval (results for the rainwater and snow concentration RF are not shown). This is an independent check on the formulation of the accumulated precipitation response function.

A comparison of the 850-hPa water vapor sensitivity and the 500-hPa PV perturbations are shown in Fig. 7 for both the 24-h accumulated precipitation and PV response functions. The water vapor sensitivity using the precipitation response function (Fig. 7a) has similar characteristics to the KE response function results (Fig. 3a). Namely, both the precipitation and KE

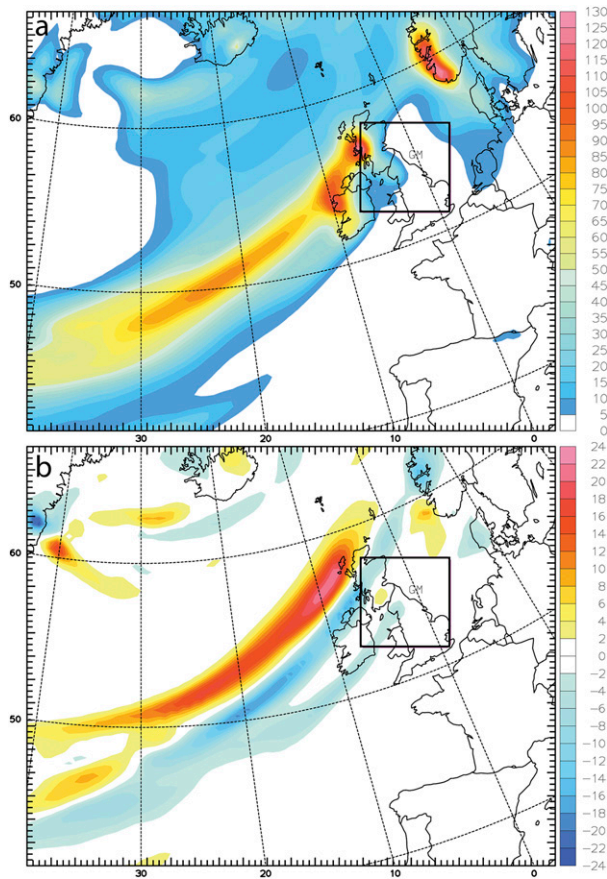


FIG. 6. Simulated precipitation shown for a subdomain region at the 48-h time valid at 0000 UTC 6 Dec 2015 for the (a) nonlinear model forecast (color shading every 5 mm), and (b) perturbation precipitation based on the optimal adjoint perturbations (color shading every 2 mm). The response function region is shown by the black box.

response functions identify key sensitive regions along the region of high water vapor associated with the AR and exhibit generally higher sensitivity along the northwestern portion of the strong water vapor gradient. Likewise, the 500-hPa PV perturbations using the precipitation RF (Fig. 7b) are similar to the sensitivities using the KE response function (Fig. 3d). The PV perturbations highlight the sensitive regions along the trough and extending northwestward over northern Canada. The precipitation RF exhibits greater sensitivity, particularly for the PV perturbation (Fig. 7b) south of the trough along the developing warm front in a region that may be an incipient warm conveyor belt. The PV perturbations generally are of opposite sign at the initial time in a banded region along the East Coast of the United States and Canada for the KE RF and precipitation RF experiments. Both experiments exhibit rapid perturbation growth in magnitude and vertical

extent. The optimal perturbations evolve quite differently for the two different RFs (KE and precipitation). For the precipitation RF experiment, the negative PV perturbation regions trigger a more intense development of a PV anomaly just northwest of the United Kingdom at the 24-h forecast time relative to the KE RF experiments. This PV anomaly then contributes to a southward shift in the frontal zone and enhancement of the precipitation in the RF region at the final time (48 h) in the precipitation RF experiment.

The water vapor sensitivity and PV perturbations using the PV response function (note the PV response function box is located to the SE of the United Kingdom in a region of strong low-level PV), shown in Figs. 7c and 7d, respectively, highlight the moisture plume and trough regions along the western Atlantic, broadly similar in character to the KE and precipitation RF results. The 850-hPa water vapor sensitivity for the PV response function (Fig. 7c) does highlight a low-level region of strong sensitivity along the west coast of Greenland associated with lee cyclogenesis.

The evolved optimal perturbations for the accumulated precipitation and 850-hPa PV fields are shown in Fig. 8 for the precipitation and PV RF experiments. Not surprisingly, the accumulated precipitation perturbation is increased substantially in the RF box for the precipitation RF experiment (Fig. 8a), in contrast to the PV RF experiment (Fig. 8c) in which the precipitation perturbation remains quite small. The precipitation RF experiment enhances the strong low-level moisture convergence present in the nonlinear simulation at the 48-h time (Fig. 9a). The frontal and moisture convergence maxima are shifted south (Fig. 9b) and enhance the precipitation over northwestern England and southern Scotland in better agreement with the observations (Fig. 2). The precipitation RF experiment is a clear improvement over the KE RF results for precipitation (Fig. 6b), which actually decreased the precipitation in the RF box.

The evolved PV perturbations for the precipitation (Fig. 8b) and PV (Fig. 8d) RFs differ substantially. The PV RF results (Fig. 8d) show a perturbation PV dipole with an overall net increase in the RF box by ~ 0.25 PVU ($1 \text{ PVU} = 10^{-6} \text{ K kg}^{-1} \text{ m}^2 \text{ s}^{-1}$) along the frontal PV streamer at 850 hPa that results in a shift in the frontal position and associated low-level PV field. The precipitation RF results show that these perturbations only have a minor impact on the PV distribution (Fig. 8b). These results show how the optimal perturbations are indeed constructed to modify the specific response function, and initial perturbations that may be in similar general locations but of different specific structures can evolve very differently (similar to the results found in Reynolds et al. 2019).

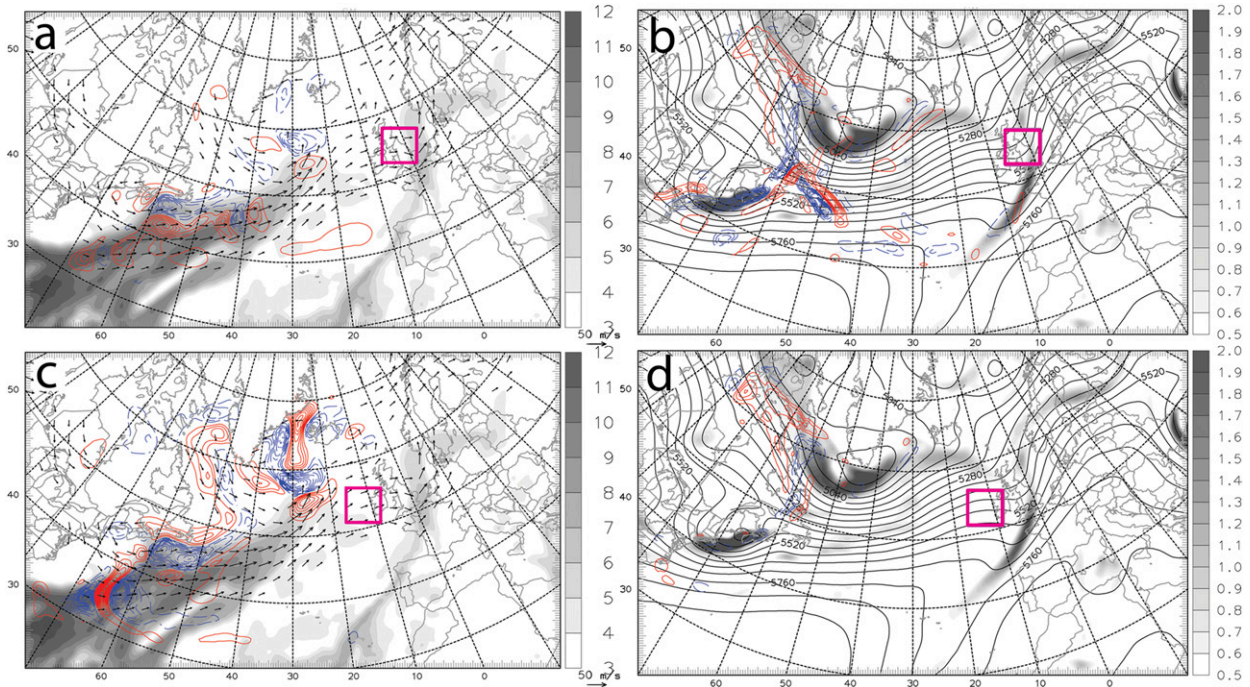


FIG. 7. Horizontal plan views of the initial condition and sensitivity fields valid at 0000 UTC 4 Dec 2015 using (a),(b) an accumulated precipitation (24 h) response function and (c),(d) potential vorticity response function. The response function locations are shown by the magenta boxes. (a) 850-hPa water vapor (g kg^{-1} in gray shading intervals every 1 g kg^{-1}), 850-hPa water vapor sensitivity [positive (red) and negative (blue) contours with an interval of $0.03 \text{ m}^2 \text{ s}^{-2} (\text{g kg}^{-1})^{-1}$], and 850-hPa wind vectors greater than 15 m s^{-1} (every sixth grid point), (b) 500-hPa potential vorticity (PVU in gray shading intervals every 0.1 PVU), 500-hPa geopotential every 60 m (black contours), and the 500-hPa PV perturbations [positive (red) and negative (blue) contours with interval every 0.01 PVU], (c) as in (a), but using the potential vorticity response function, and (d) as in (b), but using the potential vorticity response function. The sensitivities in (a),(c) are scaled by $10^5 \text{ km}^3/(\Delta x \Delta y \Delta z)$.

d. Optimal perturbation spectral characteristics and energetics

Power spectra for the perturbation zonal wind at 1740 m, shown in Fig. 10, highlight some of the key characteristics exhibited by the adjoint optimal perturbation evolution. Zonal slices over the domain are analyzed, excluding the two outermost boundary points, and are shown every 6 h as the perturbations are evolved using the tangent linear model. The initial-time perturbation energy peaks at a $\sim 700 \text{ km}$ wavelength with a secondary maximum near $\sim 1300 \text{ km}$. Perturbation growth overall occurs rapidly and generally exhibits little up-scale shift in the spectrum peak that remains at $\sim 1200\text{--}1400 \text{ km}$ wavelength from 12 to 48 h, unlike the case analyzed by Doyle et al. (2014). This rapid growth is broadly consistent with the concept of initial unshielding (Orr 1907; Farrell 1982) of the PV anomalies, along with sloped frontal ascent and latent heating that feed back and enhance the baroclinic processes.

The domain-averaged total moist energy of the initial- and final-time optimal perturbations is shown in Fig. 11. The total moist energy is computed following

Ehrendorfer et al. (1999) and Errico et al. (2004), and is defined as

$$E = \frac{1}{2N} \left[\sum_{i,j,k} \Delta\sigma_{i,j,k} (u_{i,j,k}^2 + v_{i,j,k}^2) + \frac{C_p}{T_r} \sum_{i,j,k} \Delta\sigma_{i,j,k} T_{i,j,k}'^2 + \frac{RT_r}{p_{sr}^2} \sum_{i,j,k} \Delta\sigma_{i,j,k} p_{i,j,k}'^2 + \varepsilon \frac{l_v^2}{C_p T_v} \sum_{i,j,k} \Delta\sigma_{i,j,k} q_{vi,j,k}'^2 \right], \quad (8)$$

where i, j, k are horizontal and vertical gridpoint indices, N is the number of points, u and v are the horizontal wind components, T is the temperature, $R = 287.04 \text{ J kg}^{-1} \text{ K}^{-1}$ is the gas constant, $C_p = 1005.7 \text{ J kg}^{-1} \text{ K}^{-1}$ is the specific heat of air at constant pressure, $T_r = 300 \text{ K}$ and $p_{sr} = 1000 \text{ hPa}$ are reference T and p_s values and a prime indicates a perturbation, T_v is the virtual temperature, q_v is the water vapor, and $l_v = 2.501 \times 10^6 \text{ J kg}^{-1}$ and is the latent of vaporization. The terms on the right-hand side of the equation correspond to the kinetic (term 1), potential (term 2), internal (term 3), and the moist (term 4) energy components. The moisture term is scaled by a factor ε , following Ehrendorfer et al. (1999) and is set to unity here, consistent with their standard case. They

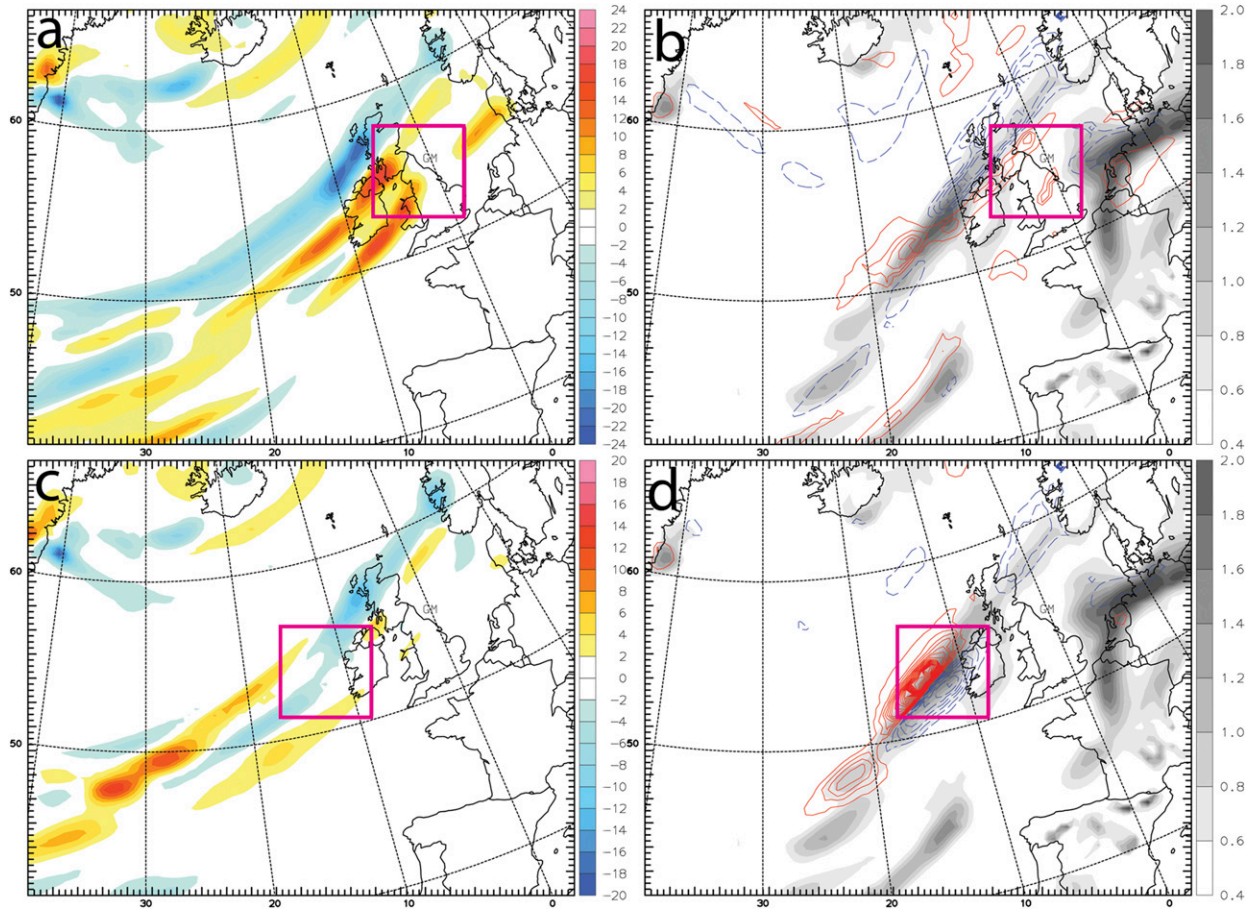


FIG. 8. Perturbation precipitation (shown for a subdomain region) based on the optimal adjoint perturbations (color shading every 2 mm) is shown for the (a) precipitation response function and (c) potential vorticity response function valid at 0000 UTC 6 Dec 2015 (48-h simulation time). The potential vorticity at 850-hPa (gray shading every 0.2 PVU) is shown with the perturbation potential vorticity at 850 hPa [positive (red) and negative (blue) contours with an interval of 0.01 PVU] for the (b) precipitation response function and (d) potential vorticity response function. The response function location is shown by the magenta box.

explore the implications of various ε values for calculation of moist singular vectors. The normalized mass in each layer is represented by $\Delta\sigma$. As described above, the scaling of the initial perturbations is consistent with the data assimilation system.

The domain-averaged total, kinetic, potential, internal and moist energies in (8) for the initial perturbations for the KE RF experiment (Fig. 11a) exhibit maxima in the 3–5 km layer. The total energy is dominated by the moist term at the initial time since the moisture sensitivity is approximately 2 and 5 times greater than temperature and wind sensitivities, respectively. During the 48-h integration, rapid perturbation growth occurs (by two orders of magnitude) as the KE term dominates, as indicated by the final time energy budget (Fig. 11b). The perturbation growth extends throughout the depth of the troposphere, with the strongest growth occurring near ~ 8 km, near the altitude of the upper-tropospheric

jet. The simulations using the precipitation RF exhibit generally similar energetics characteristics in terms of the overall growth and perturbation maxima at the final time near the jet level.

A time series of the total dry energy evolution during the tangent linear simulation is shown for the KE response function and precipitation response function in Fig. 12. The total energy for both the KE and precipitation response function experiments grows rapidly in the first 3 h of the simulation, followed by a slower but steady growth period for the remainder of the 48-h simulation. The KE response function using just momentum optimal perturbations at the initial time do not exhibit the rapid early growth and increase steadily with an indication of saturation near the end of the 48-h simulation. In contrast, the KE response function using only the moisture perturbations induces a large response in the wind and temperature fields in the first 3 h and

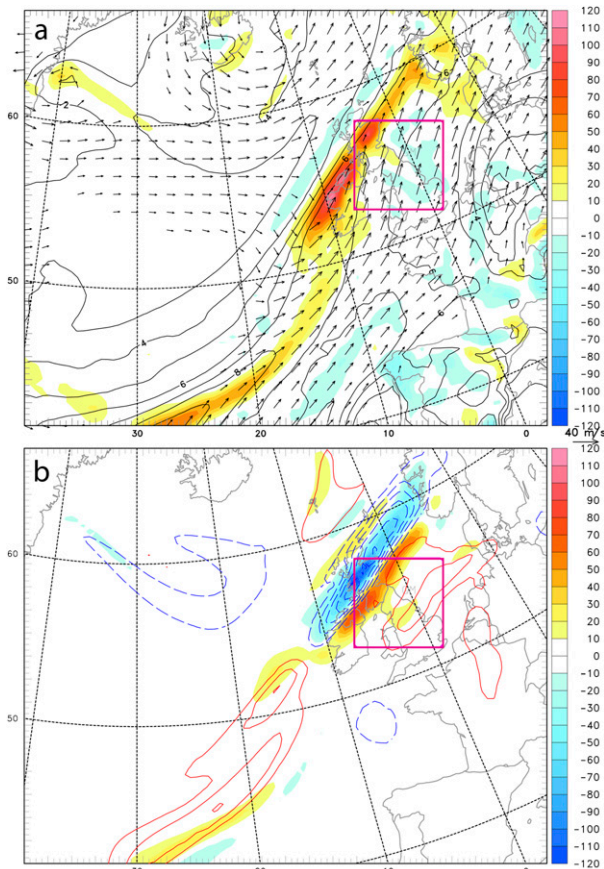


FIG. 9. Moisture convergence using the precipitation response function at 900 hPa valid at 6 Dec 2015 (48-h simulation time) over a subdomain for the (a) 900-hPa nonlinear model moisture convergence [color shading interval every $10 \times 10^{-5} \text{ g (kg s}^{-1})$], 900-hPa wind vectors (every 3 grid points) for wind speeds greater than 10 m s^{-1} , and 900-hPa water vapor (black contours every 1 g kg^{-1}) and (b) 900-hPa perturbation moisture convergence [color shading interval every $10 \times 10^{-5} \text{ g (kg s}^{-1})$], and 900-hPa perturbation water vapor [positive (red) and negative (blue) contours with an interval of 0.5 g kg^{-1}]. The response function location is shown by the magenta box.

exhibits a rapid total energy growth by the end of the 48-h simulation, although approximately 3 times less than the full perturbation experiment. Similar growth characteristics are found for tropical phenomena as well, as shown in an adjoint sensitivity study of tropical cyclone Kelvin wave interactions by Reynolds et al. (2016). The results underscore the importance of the moist optimal perturbations and their structure relative to the momentum and temperature perturbations for the initial rapid growth rate and overall growth.

4. Sensitivity in the North Atlantic storm track during winter 2013/14

In this section, the adjoint sensitivity during the record-setting winter of 2013/14 over the United Kingdom and

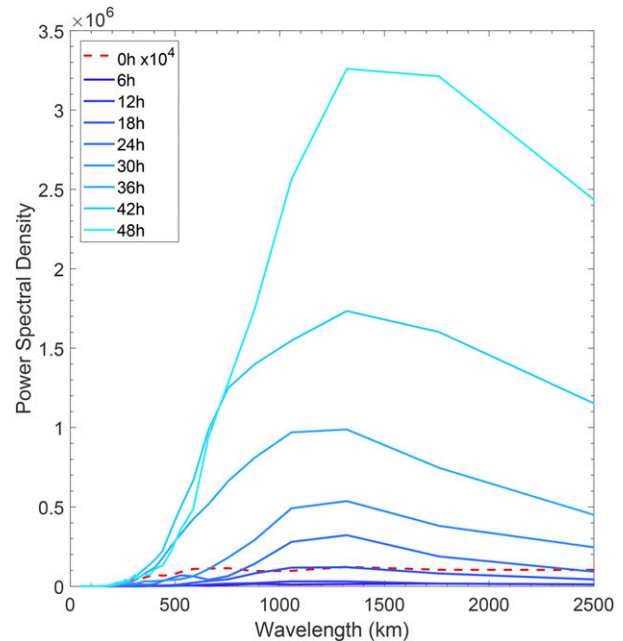


FIG. 10. Power spectral density ($\times 10^6$) ($\text{m}^3 \text{ s}^{-2}$) for the u -wind component adjoint optimal perturbations at 1740 m shown every 6 h over the 48-h integration. The darker blue colors correspond to the earlier times in the integration, and lighter blue denotes the later times. The red dashed line represents the spectrum at the initial time, scaled by 10^4 .

North Atlantic is examined. The winter of 2013/14 was exceptionally active over the North Atlantic, with at least 12 major winter storms affecting the United Kingdom (Met Office, <https://www.metoffice.gov.uk/climate/uk/summaries/2014/winter>). It was the wettest winter in the U.K.'s observational records (including from the perspective of the long running England and Wales Precipitation database dating from 1766), and the stormiest period of weather experienced for the United Kingdom over the previous two decades. There were widespread impacts in the United Kingdom, exasperated by the cumulative effect of numerous severe extratropical cyclones that occurred in rapid succession. The winter storms caused widespread disruption to transport networks and power supplies; and there were multiple fatalities with many homes and businesses flooded (Kendon and McCarthy 2015).

A series of 36-h forecasts were performed using the COAMPS adjoint modeling system with a horizontal resolution of 45 km and 40 vertical levels. The forecasts were initialized from GFS analyses and GFS forecasts were used for the lateral boundary conditions with updates to the boundary conditions occurring at a 3 h cadence. Forecasts and adjoint calculations using KE and accumulated precipitation (24–36-h forecast time period) response functions were conducted every 6 h from

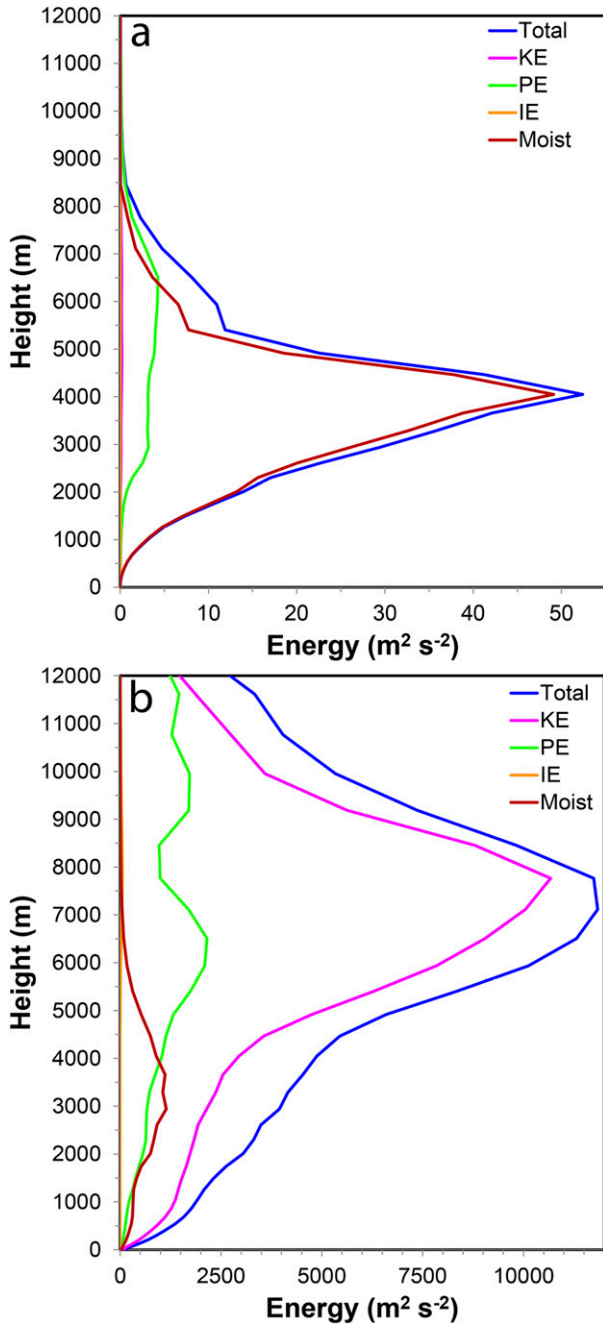


FIG. 11. Energetics diagnostics ($m^2 s^{-2}$) displaying the total energy (blue), and the kinetic energy (KE, magenta), potential energy (PE, green), internal energy (IE, orange), and moist energy (moist, red) contributions for the (a) initial time and (b) 48-h simulation time (valid at 0000 UTC 6 Dec 2015) in units of $m^2 s^{-2}$.

1 December 2013 to 28 February 2014, with the response function box centered over the United Kingdom.

The initial state 700-hPa water vapor and 250-hPa wind speed averaged over the December 2013–February 2014 time period is shown in Fig. 13. The locations of the

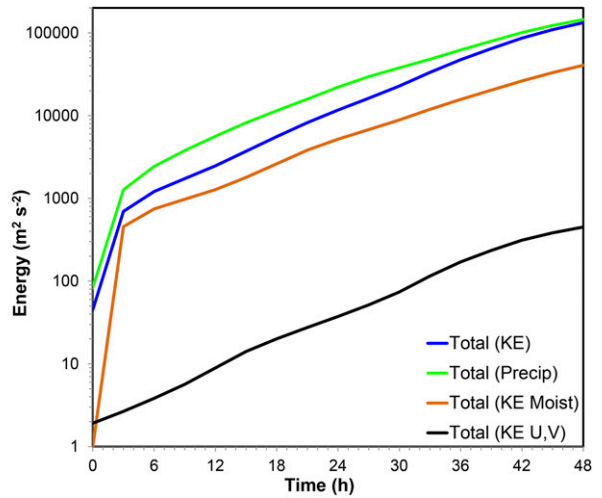


FIG. 12. A time series of the total dry energy evolution ($m^2 s^{-2}$) during the simulation is shown for the kinetic energy response function (blue), precipitation response function (green), kinetic energy response function with just initial momentum optimal perturbations (black), and kinetic energy response function with just the moisture optimal perturbations (orange).

domainwide water vapor sensitivity maxima are shown for each analysis every 6 h for the 3 month period for the KE (Fig. 13a) and accumulated precipitation (Fig. 13b) RFs. The sensitivity magnitude of the absolute value of the domainwide sensitivity maximum or minimum is denoted by the size of the triangle symbol, with larger symbols corresponding to greater sensitivity. For both the KE and precipitation response functions, the distribution of the sensitivity maxima is quite broad with the largest maxima centered primarily near the mean jet exit region and over the northern portion of the water vapor plume near the water vapor gradient and within proximity of the stronger dynamical forcing, similar to that found by Reynolds et al. (2019) for U.S. West Coast atmospheric river events. We have analyzed several cases during this time period and note that many of the most sensitive regions with respect to water vapor coincide with low-level inflow regions of warm conveyor belts (e.g., Binder et al. 2016). This will be explored further in a future study. It is also noteworthy that a number of the maxima are located more than 4000 km upstream of the United Kingdom for both RFs, indicative of the strong jet and associated dynamics. Very few of the largest sensitivity maxima are found south of the mean water vapor plume.

The relationship between strong periods of sensitivity and extratropical cyclones impacting the United Kingdom is illustrated in Fig. 14, which shows a time series of the water vapor sensitivity maximum magnitude (at the initial time) and the mean wind speed over the United Kingdom

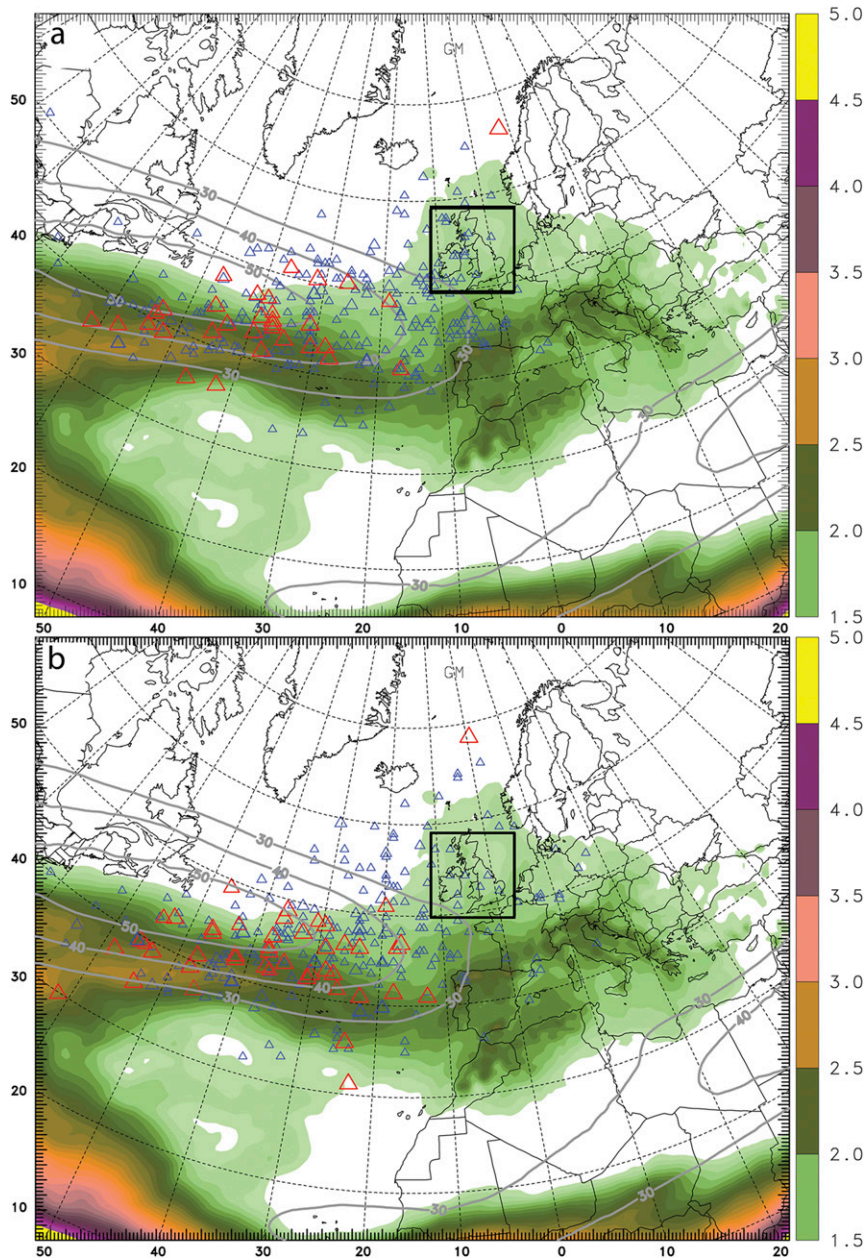


FIG. 13. Initial state 700-hPa water vapor (color shading interval of 0.5 g kg^{-1}) averaged over the December 2013 through February 2014 time period. The 250-hPa mean winds are shown by the gray contours (every 10 m s^{-1} greater than 30 m s^{-1}). The locations of the magnitude of the water vapor sensitivity maxima every 6 h are denoted by the size of the triangle symbol. The larger red (smaller blue) triangle symbols correspond to larger (smaller) sensitivity magnitudes shown for the (a) kinetic energy response function and (b) precipitation response function. The locations of the response functions are shown by the black boxes.

in the KE RF box at 36-h for the time period of 15 December 2013–16 February 2014. Although the relationship is complex, periods of strong sensitivity appear to be correlated with periods of high wind speeds over the United Kingdom, often associated with intense extratropical cyclones in the vicinity of the United Kingdom.

One of the stronger events during the winter 2013/14 occurred during 23–25 December 2013, and featured an intense extratropical cyclone positioned near the NE tip of Scotland with a central pressure of 927 hPa. This extratropical cyclone resulted in high winds with maximum gusts over 40 m s^{-1} , significant flooding across southern

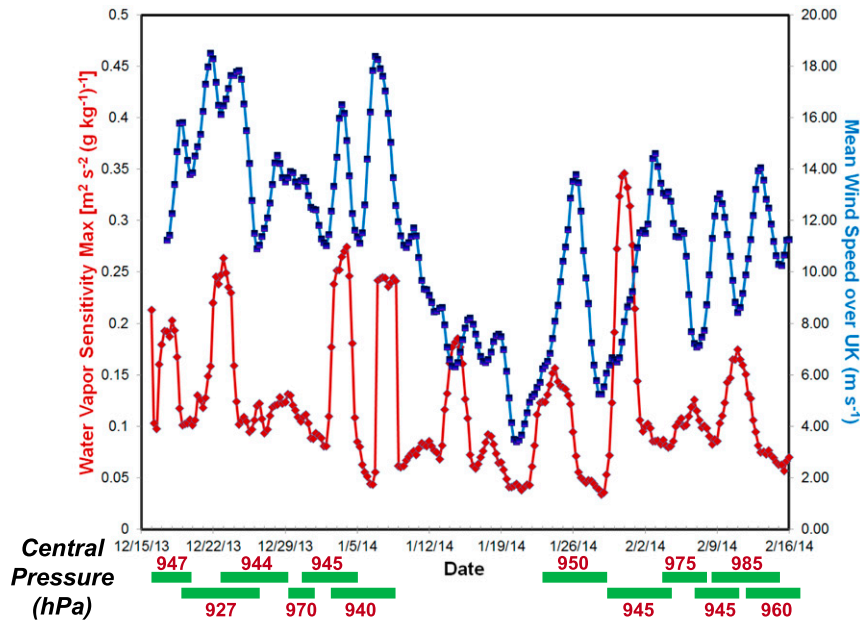


FIG. 14. Time series of the water vapor sensitivity maximum magnitude [$\text{m}^2 \text{s}^{-2} (\text{g kg}^{-1})^{-1}$] for the initial state (red) and the mean wind speed over the United Kingdom in the RF box at 36 h (blue) for the time period of 15 Dec 2013 through 16 Feb 2014. The kinetic energy response function is located in a box over the United Kingdom at the 36-h forecast time. The minimum central pressure (hPa) of significant baroclinic cyclones impacting the United Kingdom are shown along the abscissa along with the temporal extent (shown by the green lines).

England and widespread power outages (Kendon and McCarthy 2015). Figure 15 shows the initial state and water vapor sensitivity fields for the KE (Figs. 15a,b) and precipitation (Figs. 15c,d) RFs. The water vapor sensitivity at the initial time is a maximum at 700-hPa located just poleward of the atmospheric river and near a short-wave trough. Both the KE (Fig. 15a) and precipitation (Fig. 15c) RFs exhibit similar sensitivity structures. The evolved optimal perturbations for the simulations using the KE and precipitation RFs, shown in Figs. 15b and 15d, respectively, demonstrate the significance of these sensitivity structures. In the simulation using the KE RF, the 900-hPa wind speeds increase by up to 14 m s^{-1} in the RF box within the strong southerly low-level jet positioned over the United Kingdom (Fig. 15b). The simulation using the precipitation RF shows an increase in the accumulated precipitation by up to 15 mm over the United Kingdom, further enhancing the already substantial precipitation (Fig. 15d).

As was shown in Fig. 14, there is large day-to-day variability in the magnitude of the adjoint sensitivity, with large sensitivity periods often corresponding with intense cyclones. It is also of interest to see if the day-to-day variability in the magnitude of the sensitivity is related to day-to-day variability in forecast error. Applications such as adaptive observations are predicated upon the concept that enhanced sensitivity to initial

perturbations or errors will also result in an enhanced likelihood of large forecast errors. To test this hypothesis, Fig. 16 shows a scatterplot of the KE of the wind speed errors in the RF region at final time (36 h) in the COAMPS forecast (using GFS analysis as verification) versus the magnitude of the water vapor sensitivity integrated over the domain for the KE RF cases. The correlation is 0.7 between the 36-h forecast error and moisture sensitivity magnitude. Similar results (not shown) are found for the temperature and wind sensitivities, in broad agreement with the findings of Reynolds et al. (2019) for atmospheric river events. As forecast errors are due to model errors as well as initial errors, and the degree to which initial errors project onto these fast growing structures will vary from day to day, we do not expect a perfect relationship between sensitivity magnitude and forecast error. However, this high positive correlation does show that on average, larger sensitivity is associated with larger forecast error. These results support the relevance of adjoint sensitivity studies for purposes such as adaptive observing and predictability studies.

5. Summary and conclusions

We have utilized an adjoint modeling system that includes microphysics to explore the forecast sensitivity

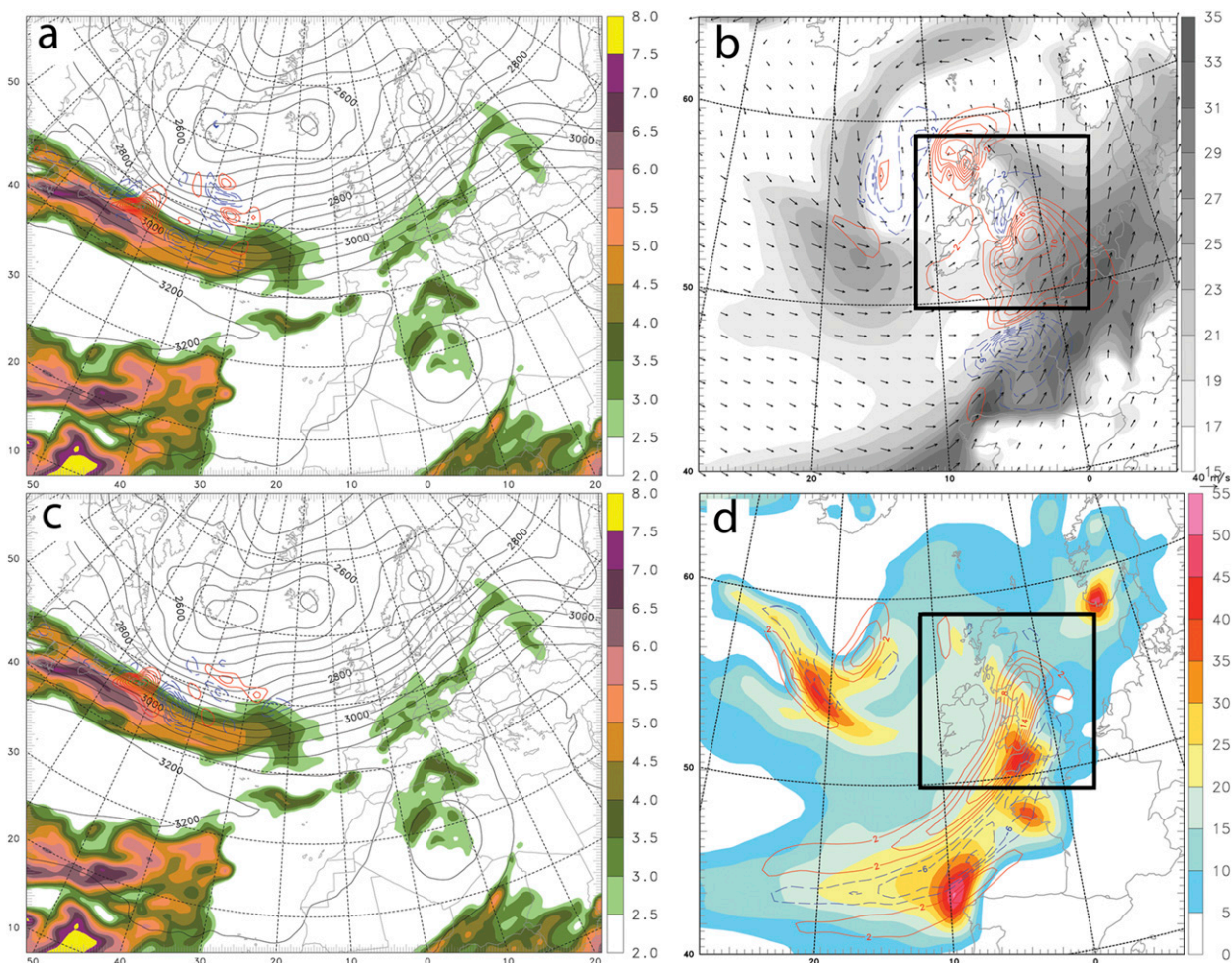


FIG. 15. Horizontal plan views of the initial condition and sensitivity fields (valid at 1800 UTC 22 Dec 2013) and 36-h forecast fields (valid at 0600 UTC 24 Dec 2013). (a) Initial state 700-hPa water vapor (g kg^{-1} in color shading intervals every 1 g kg^{-1}), 700-hPa water vapor sensitivity [red (positive) and blue (negative) contours with an interval of $0.03 \text{ m}^2 \text{ s}^{-2} (\text{g kg}^{-1})^{-1}$], and 700-hPa geopotential heights every 50 m for the sensitivity calculation using the kinetic energy response function, (b) subdomain plan view of the 36-h forecast 900-hPa wind speed (gray shading interval of 2 m s^{-1}), wind vectors every 3 grid points, and adjoint optimal wind speed perturbations [positive (red) and negative (blue) isotachs every 2 m s^{-1}] using the kinetic energy response function, (c) as in (a), but for the precipitation response function, and (d) subdomain plan view of the 36-h accumulated precipitation (color shading every 5 mm) and the adjoint precipitation perturbation field [positive (red) and negative (blue) contours every 3 mm]. The black box shows the response function location in (b),(d). The sensitivities are scaled by $10^5 \text{ km}^3/(\Delta x \Delta y \Delta z)$.

and predictability of a damaging extratropical cyclone, “Desmond,” as well as the record-setting winter of 2013/14 that features flooding and high-wind events over the United Kingdom. The moist capabilities of the adjoint modeling system using several different response functions, including KE, accumulated precipitation and PV, allow us to assess sensitivity and predictability of high-impact extratropical cyclones more completely than possible in previous studies. Desmond developed beneath a PV anomaly along an atmospheric river that featured enhanced lower- and midtropospheric water vapor, which appeared to enhance the intensification.

Analysis of the adjoint sensitivity gradients using KE, precipitation, and PV response functions indicate that

the intensity of the strong winds and heavy precipitation amounts associated with Desmond were especially sensitive to aspects of the lower- and midtropospheric water vapor fields. The sensitivity maxima for all three response functions considered are generally found along the sloped frontal region along the poleward edge of the atmospheric river. At the initial time, the optimal perturbations are oriented along the sloping front and tilted upshear, and subsequently become vertically oriented as they grow from the mean state energy, similar to that found in other studies (see Farrell 1988, 1989; Lacarra and Talagrand 1988; Borges and Hartmann 1992). The adjoint sensitivity results show that relatively confined mesoscale regions of water vapor within the AR at the

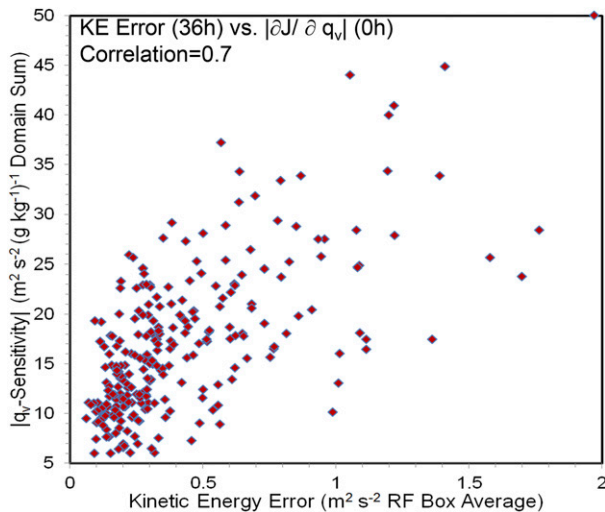


FIG. 16. Scatterplot of the kinetic energy error ($\text{m}^2 \text{s}^{-2}$) at the 36-h forecast time averaged over the response function box vs the magnitude of the water vapor sensitivity [$\text{m}^2 \text{s}^{-2} (\text{g kg}^{-1})^{-1}$] integrated over the domain. The sensitivities are scaled by $10^3 \text{ km}^3 / (\Delta x \Delta y \Delta z)$.

initial time in the incipient phase of the cyclone were critically important for the intensification of Desmond. The PV perturbations are located in an environment with strong vertical wind shear associated with an upper-level jet with an enhanced sensitivity region along the sloping frontal zone extending from the boundary layer up through the midtroposphere.

Perturbations are created based on the adjoint sensitivity with initial magnitudes comparable to analysis errors, and evolved using the nonlinear and tangent linear models. These optimal perturbations grow rapidly throughout the 48 h forecast, resulting in 10-m wind speed perturbations at 900 hPa in excess of 15 m s^{-1} using the KE RF and precipitation perturbations of over 20 mm using the precipitation RF. The perturbations are characterized by a maximum in the total energy in the lower to midtroposphere that rapidly extend vertically and grow through the depth of the troposphere. The total energy using the KE RF is dominated by the moist contributions at the initial time, while KE is dominant by the final time. Water vapor optimal perturbations grow nearly as rapidly as perturbations to the entire state vector and result in evolved dry total energy perturbations that are much larger than those produced using only the wind optimal perturbations. The power spectrum for the perturbation u-wind component shows rapid growth in the case of Desmond, with little evidence of an upscale energy transfer during the forecast in contrast to the extratropical cyclone Xynthia examined by Doyle et al. (2014).

The adjoint results highlight the sensitivity of strong winds within the low-level jets and heavy precipitation

areas to upstream regions of water vapor, often located near atmospheric rivers and low-level inflow regions of warm conveyor belts. The results highlight the possibility of scenarios with even stronger low-level winds and greater precipitation amounts than were actually realized. The results suggest the need for higher-fidelity moisture observations and advanced data assimilation systems that have the capability to analyze faithfully finescale gradients of moisture. However, the intrinsic predictability of the high-impact weather associated with these extratropical cyclones may be limited given the potential for rapid perturbation and error growth.

Acknowledgments. This research is supported by the Chief of Naval Research through the NRL Base Program, PE 0601153N. We thank Matt Fearon of the National Research Council for providing Fig. 2. We gratefully acknowledge the insightful comments and suggestions of Brett Hoover and Hanin Binder, as well as an anonymous reviewer. Computational resources were supported by a grant of High Performance Computing time from the Navy DoD Supercomputing Resource Center (DSRC), Stennis Space Center, MS. The COAMPS system is a registered trademark of the Naval Research Laboratory.

REFERENCES

- Amerault, C., X. Zou, and J. D. Doyle, 2008: Tests of an adjoint mesoscale model with explicit moist physics on the cloud scale. *Mon. Wea. Rev.*, **136**, 2120–2132, <https://doi.org/10.1175/2007MWR2259.1>.
- Ancell, B. C., and C. F. Mass, 2006: Structure, growth rates, and tangent linear accuracy of adjoint sensitivities with respect to horizontal and vertical resolution. *Mon. Wea. Rev.*, **134**, 2971–2988, <https://doi.org/10.1175/MWR3227.1>.
- , and —, 2008: The variability of adjoint sensitivity with respect to model physics and basic-state trajectory. *Mon. Wea. Rev.*, **136**, 4612–4628, <https://doi.org/10.1175/2008MWR2517.1>.
- Badger, J., and B. J. Hoskins, 2001: Simple initial value problems and mechanisms for baroclinic growth. *J. Atmos. Sci.*, **58**, 38–49, [https://doi.org/10.1175/1520-0469\(2001\)058<0038:SIVPAM>2.0.CO;2](https://doi.org/10.1175/1520-0469(2001)058<0038:SIVPAM>2.0.CO;2).
- Bauer, P., A. Thorpe, and G. Brunet, 2015: The quiet revolution of numerical weather prediction. *Nature*, **525**, 47–55, <https://doi.org/10.1038/nature14956>.
- Binder, H., M. Boettcher, H. Joos, and H. Wernli, 2016: The role of warm conveyor belts for the intensification of extratropical cyclones in Northern Hemisphere winter. *J. Atmos. Sci.*, **73**, 3997–4020, <https://doi.org/10.1175/JAS-D-15-0302.1>.
- Borges, M., and D. L. Hartmann, 1992: Barotropic instability and optimal perturbations of observed non-zonal flows. *J. Atmos. Sci.*, **49**, 335–354, [https://doi.org/10.1175/1520-0469\(1992\)049<0335:BIAOPO>2.0.CO;2](https://doi.org/10.1175/1520-0469(1992)049<0335:BIAOPO>2.0.CO;2).
- Browning, K. A., 1990: Organization of clouds and precipitation in extratropical cyclones. *Extratropical Cyclones: The Erik Palmén*

- Memorial Volume*, C. W. Newton and E. O. Holopainen, Eds., Amer. Meteor. Soc., 129–153.
- , M. E. Hardman, T. W. Harrold, and C. W. Pardoe, 1973: Structure of rainbands within a mid-latitude depression. *Quart. J. Roy. Meteor. Soc.*, **99**, 215–231, <https://doi.org/10.1002/qj.49709942002>.
- Buizza, R., and T. N. Palmer, 1995: The singular-vector structure of the atmospheric general circulation. *J. Atmos. Sci.*, **52**, 1434–1456, [https://doi.org/10.1175/1520-0469\(1995\)052<1434:TSVSOT>2.0.CO;2](https://doi.org/10.1175/1520-0469(1995)052<1434:TSVSOT>2.0.CO;2).
- Carlson, T. N., 1980: Airflow through midlatitude cyclones and the comma cloud pattern. *Mon. Wea. Rev.*, **108**, 1498–1509, [https://doi.org/10.1175/1520-0493\(1980\)108<1498:ATMCAT>2.0.CO;2](https://doi.org/10.1175/1520-0493(1980)108<1498:ATMCAT>2.0.CO;2).
- Coutinho, M. M., B. J. Hoskins, and R. Buizza, 2004: The influence of physical processes on extratropical singular vectors. *J. Atmos. Sci.*, **61**, 195–209, [https://doi.org/10.1175/1520-0469\(2004\)061<0195:TIOppo>2.0.CO;2](https://doi.org/10.1175/1520-0469(2004)061<0195:TIOppo>2.0.CO;2).
- Davis, C. A., M. T. Stoelinga, and Y.-H. Kuo, 1993: The integrated effect of condensation in numerical simulations of extratropical cyclogenesis. *Mon. Wea. Rev.*, **121**, 2309–2330, [https://doi.org/10.1175/1520-0493\(1993\)121<2309:TIEOCI>2.0.CO;2](https://doi.org/10.1175/1520-0493(1993)121<2309:TIEOCI>2.0.CO;2).
- Dijkstra, T., K. Freeborough, H. Reeves, B. S. Nykjaer, M. Sund, G. Devoli, and V. Banks, 2016: Landslide response signatures from storm Desmond (UK)/Synne (Norway), December 2015. *EGU General Assembly Conf. Abstracts*, Vienna Austria, EGU, EPSC2016-16411.
- Doyle, J. D., C. A. Reynolds, C. Amerault, and J. Moskaitis, 2012: Adjoint sensitivity and predictability of tropical cyclogenesis. *J. Atmos. Sci.*, **69**, 3535–3557, <https://doi.org/10.1175/JAS-D-12-0110.1>.
- , C. Amerault, C. A. Reynolds, and P. A. Reinecke, 2014: Initial condition sensitivity and predictability of a severe extratropical cyclone using a moist adjoint. *Mon. Wea. Rev.*, **142**, 320–342, <https://doi.org/10.1175/MWR-D-13-00201.1>.
- Durrán, D. R., P. A. Reinecke, and J. D. Doyle, 2013: Large-scale errors and mesoscale predictability in Pacific Northwest Snowstorms. *J. Atmos. Sci.*, **70**, 1470–1487, <https://doi.org/10.1175/JAS-D-12-0202.1>.
- Ehrendorfer, M., R. Errico, and K. Raeder, 1999: Singular vector perturbation growth in a primitive equation model with moist physics. *J. Atmos. Sci.*, **56**, 1627–1648, [https://doi.org/10.1175/1520-0469\(1999\)056<1627:SVPGIA>2.0.CO;2](https://doi.org/10.1175/1520-0469(1999)056<1627:SVPGIA>2.0.CO;2).
- Enz, R., P. Zimmerli, and S. Schwartz, 2009: Natural catastrophes and man-made disasters in 2008: North America and Asia suffer heavy losses. Swiss Reinsurance Co. Ltd., Zurich, Switzerland, 43 pp., https://www.preventionweb.net/files/8841_Sigma22009e.pdf.
- Errico, R. M., 1997: What is an adjoint model? *Bull. Amer. Meteor. Soc.*, **78**, 2577–2591, [https://doi.org/10.1175/1520-0477\(1997\)078<2577:WIAAM>2.0.CO;2](https://doi.org/10.1175/1520-0477(1997)078<2577:WIAAM>2.0.CO;2).
- , and T. Vukicevic, 1992: Sensitivity analysis using an adjoint of the PSU-NCAR mesoscale model. *Mon. Wea. Rev.*, **120**, 1644–1660, [https://doi.org/10.1175/1520-0493\(1992\)120<1644:SAUAAO>2.0.CO;2](https://doi.org/10.1175/1520-0493(1992)120<1644:SAUAAO>2.0.CO;2).
- , and K. D. Raeder, 1999: An examination of the accuracy of the linearization of a mesoscale model with moist physics. *Quart. J. Roy. Meteor. Soc.*, **125**, 169–195, <https://doi.org/10.1002/qj.49712555310>.
- , —, and L. Fillion, 2003: Examination of the sensitivity of forecast precipitation rates to possible perturbations of initial conditions. *Tellus*, **55A**, 88–105, <https://doi.org/10.3402/tellusa.v55i1.12083>.
- , —, and M. Ehrendorfer, 2004: Singular vectors for moisture-measuring norms. *Quart. J. Roy. Meteor. Soc.*, **130**, 963–987, <https://doi.org/10.1256/qj.02.227>.
- Farrell, B. F., 1982: The initial growth of disturbances in a baroclinic flow. *J. Atmos. Sci.*, **39**, 1663–1686, [https://doi.org/10.1175/1520-0469\(1982\)039<1663:TIGODI>2.0.CO;2](https://doi.org/10.1175/1520-0469(1982)039<1663:TIGODI>2.0.CO;2).
- , 1988: Optimal excitation of neutral Rossby waves. *J. Atmos. Sci.*, **45**, 163–172, [https://doi.org/10.1175/1520-0469\(1988\)045<0163:OEONRW>2.0.CO;2](https://doi.org/10.1175/1520-0469(1988)045<0163:OEONRW>2.0.CO;2).
- , 1989: Optimal excitation of baroclinic waves. *J. Atmos. Sci.*, **46**, 1193–1206, [https://doi.org/10.1175/1520-0469\(1989\)046<1193:OEOWB>2.0.CO;2](https://doi.org/10.1175/1520-0469(1989)046<1193:OEOWB>2.0.CO;2).
- Fink, A. H., T. Brücher, V. Ermert, A. Krüger, and J. G. Pinto, 2009: The European storm Kyrill in January 2007: Synoptic evolution, meteorological impacts and some considerations with respect to climate change. *Nat. Hazards Earth Syst. Sci.*, **9**, 405–423, <https://doi.org/10.5194/nhess-9-405-2009>.
- Frame, T. H. A., J. Methven, N. M. Roberts, and H. A. Tittley, 2015: Predictability of frontal waves and cyclones. *Wea. Forecasting*, **30**, 1291–1302, <https://doi.org/10.1175/WAF-D-15-0039.1>.
- Gelaro, R., R. Buzza, T. N. Palmer, and E. Klinker, 1998: Sensitivity analysis of forecast errors and the construction of optimal perturbations using singular vectors. *J. Atmos. Sci.*, **55**, 1012–1037, [https://doi.org/10.1175/1520-0469\(1998\)055<1012:SAOFEA>2.0.CO;2](https://doi.org/10.1175/1520-0469(1998)055<1012:SAOFEA>2.0.CO;2).
- , R. H. Langland, G. D. Rohaly, and T. E. Rosmond, 1999: An assessment of the singular-vector approach to targeted observing using the FASTEX data set. *Quart. J. Roy. Meteor. Soc.*, **125**, 3299–3328, <https://doi.org/10.1002/qj.49712556109>.
- Grams, C. M., and Coauthors, 2011: The key role of diabatic processes in modifying the upper tropospheric wave guide: A North Atlantic case-study. *Quart. J. Roy. Meteor. Soc.*, **137**, 2174–2193, <https://doi.org/10.1002/qj.891>.
- Harrold, T. W., 1973: Mechanisms influencing the distribution of precipitation within baroclinic disturbances. *Quart. J. Roy. Meteor. Soc.*, **99**, 232–251, <https://doi.org/10.1002/qj.49709942003>.
- Haylock, M. R., 2011: European extra-tropical storm damage risk from a multi-model ensemble of dynamically-downscaled global climate models. *Nat. Hazards Earth Syst. Sci.*, **11**, 2847–2857, <https://doi.org/10.5194/nhess-11-2847-2011>.
- Hodur, R. M., 1997: The Naval Research Laboratory's Coupled Ocean/Atmosphere Mesoscale Prediction System (COAMPS). *Mon. Wea. Rev.*, **125**, 1414–1430, [https://doi.org/10.1175/1520-0493\(1997\)125<1414:TNRLSC>2.0.CO;2](https://doi.org/10.1175/1520-0493(1997)125<1414:TNRLSC>2.0.CO;2).
- Holdaway, D., R. Errico, R. Gelaro, and J. G. Kim, 2014: Inclusion of linearized moist physics in NASA's Goddard Earth Observing System Data Assimilation Tools. *Mon. Wea. Rev.*, **142**, 414–433, <https://doi.org/10.1175/MWR-D-13-00193.1>.
- Hoover, B. T., and M. C. Morgan, 2011: Dynamical sensitivity analysis of tropical cyclone steering using an adjoint model. *Mon. Wea. Rev.*, **139**, 2761–2775, <https://doi.org/10.1175/MWR-D-10-05084.1>.
- Hoskins, B. J., and M. M. Coutinho, 2005: Moist singular vectors and the predictability of some high impact European cyclones. *Quart. J. Roy. Meteor. Soc.*, **131**, 581–601, <https://doi.org/10.1256/qj.04.48>.
- Jung, T., E. Klinker, and S. Uppala, 2004: Reanalysis and reforecast of three major European storms of the twentieth century using the ECMWF forecasting system. Part I: Analyses and deterministic forecasts. *Meteor. Appl.*, **11**, 343–361, <https://doi.org/10.1017/S1350482704001434>.

- Kendon, M., and M. McCarthy, 2015: The UK's wet and stormy winter of 2013/2014. *Weather*, **70**, 40–47, <https://doi.org/10.1002/wea.2465>.
- Kleist, D. T., and M. C. Morgan, 2005a: Application of adjoint-derived forecast sensitivities to the 24–25 January 2000 U.S. East Coast snowstorm. *Mon. Wea. Rev.*, **133**, 3148–3175, <https://doi.org/10.1175/MWR3023.1>.
- , and —, 2005b: Interpretation of the structure and evolution of adjoint-derived forecast sensitivity gradients. *Mon. Wea. Rev.*, **133**, 466–484, <https://doi.org/10.1175/MWR-2865.1>.
- Klemp, J., and R. Wilhelmson, 1978: The simulation of three-dimensional convective storm dynamics. *J. Atmos. Sci.*, **35**, 1070–1096, [https://doi.org/10.1175/1520-0469\(1978\)035<1070:TSOTDC>2.0.CO;2](https://doi.org/10.1175/1520-0469(1978)035<1070:TSOTDC>2.0.CO;2).
- Kuo, Y.-H., M. A. Shapiro, and E. G. Donall, 1991: The interaction between baroclinic and diabatic processes in a numerical simulation of a rapidly intensifying extratropical marine cyclone. *Mon. Wea. Rev.*, **119**, 368–384, [https://doi.org/10.1175/1520-0493\(1991\)119<0368:TIBBAD>2.0.CO;2](https://doi.org/10.1175/1520-0493(1991)119<0368:TIBBAD>2.0.CO;2).
- Lacarra, J.-F., and O. Talagrand, 1988: Short range evolution of small perturbations in a barotropic model. *Tellus*, **40A**, 81–95, <https://doi.org/10.1111/j.1600-0870.1988.tb00408.x>.
- Langland, R. H., and Coauthors, 1999: The North Pacific Experiment (NORPEX98): Targeted observations for improved North American weather forecasts. *Bull. Amer. Meteor. Soc.*, **80**, 1363–1384, [https://doi.org/10.1175/1520-0477\(1999\)080<1363:TNPENT>2.0.CO;2](https://doi.org/10.1175/1520-0477(1999)080<1363:TNPENT>2.0.CO;2).
- , M. A. Shapiro, and R. Gelaro, 2002: Initial condition sensitivity and error growth in forecasts of the 25 January 2000 East Coast snowstorm. *Mon. Wea. Rev.*, **130**, 957–974, [https://doi.org/10.1175/1520-0493\(2002\)130<0957:ICSAEG>2.0.CO;2](https://doi.org/10.1175/1520-0493(2002)130<0957:ICSAEG>2.0.CO;2).
- Lavers, D. A., and G. Villarini, 2013: The nexus between atmospheric rivers and extreme precipitation across Europe. *Geophys. Res. Lett.*, **40**, 3259–3264, <https://doi.org/10.1002/grl.50636>.
- , R. P. Allan, E. F. Wood, G. Villarini, D. J. Brayshaw, and A. J. Wade, 2011: Winter floods in Britain are connected to atmospheric rivers. *Geophys. Res. Lett.*, **38**, L23803, <https://doi.org/10.1029/2011GL049783>.
- , F. Pappenberger, D. S. Richardson, and E. Zsoter, 2016: ECMWF Extreme Forecast Index for water vapor transport: A forecast tool for atmospheric rivers and extreme precipitation. *Geophys. Res. Lett.*, **43**, 11 852–11 858, <https://doi.org/10.1002/2016GL071320>.
- , M. J. Rodwell, D. S. Richardson, F. M. Ralph, J. D. Doyle, C. A. Reynolds, V. Tallapragada, and F. Pappenberger, 2018: The gauging and modeling of rivers in the sky. *Geophys. Res. Lett.*, **45**, 7828–7834, <https://doi.org/10.1029/2018GL079019>.
- Leutbecher, M., J. Barkmeijer, T. N. Palmer, and A. J. Thorpe, 2002: Potential improvement to forecasts of two severe storms using targeted observations. *Quart. J. Roy. Meteor. Soc.*, **128**, 1641–1670, <https://doi.org/10.1002/qj.200212858313>.
- Liberato, M. L. R., J. G. Pinto, R. M. Trigo, P. Ludwig, P. Ordóñez, D. Yuen, and I. F. Trigo, 2013: Explosive development of winter storm Xynthia over the southeastern North Atlantic Ocean. *Nat. Hazards Earth Syst. Sci.*, **13**, 2239–2251, <https://doi.org/10.5194/nhess-13-2239-2013>.
- Louis, J. F., 1979: A parametric model of vertical eddy fluxes in the atmosphere. *Bound.-Layer Meteor.*, **17**, 187–202, <https://doi.org/10.1007/BF00117978>.
- Mahfouf, J.-F., 1999: Influence of physical processes of the tangent-linear approximation. *Tellus*, **51A**, 147–166, <https://doi.org/10.3402/tellusa.v51i2.12312>.
- , and B. Bilodeau, 2007: Adjoint sensitivity of surface precipitation to initial conditions. *Mon. Wea. Rev.*, **135**, 2879–2896, <https://doi.org/10.1175/MWR3439.1>.
- Majumdar, S., 2016: A review of targeted observations. *Bull. Amer. Meteor. Soc.*, **97**, 2287–2303, <https://doi.org/10.1175/BAMS-D-14-00259.1>.
- Martius, O., C. Schwierz, and H. C. Davies, 2010: Tropopause-level waveguides. *J. Atmos. Sci.*, **67**, 866–879, <https://doi.org/10.1175/2009JAS2995.1>.
- Massacand, A. C., H. Wernli, and H. C. Davies, 2001: Influence of upstream diabatic heating upon an alpine event of heavy precipitation. *Mon. Wea. Rev.*, **129**, 2822–2828, [https://doi.org/10.1175/1520-0493\(2001\)129<2822:IOUDHU>2.0.CO;2](https://doi.org/10.1175/1520-0493(2001)129<2822:IOUDHU>2.0.CO;2).
- Matthews, T., C. Murphy, G. McCarthy, C. Broderick, and R. L. Wilby, 2018: Super storm Desmond: A process based assessment. *Environ. Res. Lett.*, **13**, 014024, <https://doi.org/10.1088/1748-9326/aa98c8>.
- McCarthy, M., S. Spillane, S. Walsh, and M. Kendon, 2016: The meteorology of the exceptional winter of 2015/2016 across the UK and Ireland. *Weather*, **71**, 305–313, <https://doi.org/10.1002/wea.2823>.
- Molinari, J., 1985: General form of Kuo's cumulus parameterization. *Mon. Wea. Rev.*, **113**, 1411–1416, [https://doi.org/10.1175/1520-0493\(1985\)113<1411:AGFOKC>2.0.CO;2](https://doi.org/10.1175/1520-0493(1985)113<1411:AGFOKC>2.0.CO;2).
- Molteni, F., and T. Palmer, 1993: Predictability and finite-time instability of the northern winter circulation. *Quart. J. Roy. Meteor. Soc.*, **119**, 269–298, <https://doi.org/10.1002/qj.49711951004>.
- Morgan, M. C., 2001: A potential vorticity and wave activity diagnosis of optimal perturbation evolution. *J. Atmos. Sci.*, **58**, 2518–2544, [https://doi.org/10.1175/1520-0469\(2001\)058<2518:APVAWA>2.0.CO;2](https://doi.org/10.1175/1520-0469(2001)058<2518:APVAWA>2.0.CO;2).
- , 2018: On the dynamics of adjustment in the f -plane shallow water adjoint system. *J. Atmos. Sci.*, **75**, 1571–1585, <https://doi.org/10.1175/JAS-D-17-0100.1>.
- Neiman, P. J., F. M. Ralph, G. A. Wick, Y.-H. Kuo, T.-K. Wee, Z. Ma, G. H. Taylor, and M. D. Dettinger, 2008: Diagnosis of an intense atmospheric river impacting the Pacific Northwest: Storm summary and offshore vertical structure observed with COSMIC satellite retrievals. *Mon. Wea. Rev.*, **136**, 4398–4420, <https://doi.org/10.1175/2008MWR2550.1>.
- Oortwijn, J., and J. Barkmeijer, 1995: Perturbations that optimally trigger weather regimes. *J. Atmos. Sci.*, **52**, 3932–3944, [https://doi.org/10.1175/1520-0469\(1995\)052<3932:PTOTWR>2.0.CO;2](https://doi.org/10.1175/1520-0469(1995)052<3932:PTOTWR>2.0.CO;2).
- Orr, W. McF., 1907: Stability or instability of the steady motions of a perfect liquid. *Proc. Roy. Irish Acad.*, **21**, 9–69.
- Parker, D. J., and A. J. Thorpe, 1995: Conditional convective heating in a baroclinic atmosphere: A model of convective frontogenesis. *J. Atmos. Sci.*, **52**, 1699–1711, [https://doi.org/10.1175/1520-0469\(1995\)052<1699:CCHIAB>2.0.CO;2](https://doi.org/10.1175/1520-0469(1995)052<1699:CCHIAB>2.0.CO;2).
- Pinto, J. G., M. K. Karremann, K. Born, P. M. Della-Marta, and M. Klawa, 2012: Loss potentials associated with European windstorms under future climate conditions. *Climate Res.*, **54**, 1–20, <https://doi.org/10.3354/cr01111>.
- Rabier, F., E. Klinker, P. Courtier, and A. Hollingsworth, 1996: Sensitivity of forecast errors to initial conditions. *Quart. J. Roy. Meteor. Soc.*, **122**, 121–150, <https://doi.org/10.1002/qj.49712252906>.
- Ralph, F. M., P. J. Neiman, and G. A. Wick, 2004: Satellite and CALJET aircraft observations of atmospheric rivers over the eastern North Pacific Ocean during the winter of 1997/98. *Mon. Wea. Rev.*, **132**, 1721–1745, [https://doi.org/10.1175/1520-0493\(2004\)132<1721:SACAOO>2.0.CO;2](https://doi.org/10.1175/1520-0493(2004)132<1721:SACAOO>2.0.CO;2).

- , —, G. N. Kiladis, K. Weickmann, and D. W. Reynolds, 2011: A multiscale observational case study of a Pacific atmospheric river exhibiting tropical–extratropical connections and a mesoscale frontal wave. *Mon. Wea. Rev.*, **139**, 1169–1189, <https://doi.org/10.1175/2010MWR3596.1>.
- , M. D. Dettinger, M. M. Cairns, T. J. Galarneau, and J. Eylander, 2018: Defining “atmospheric river”: How the *Glossary of Meteorology* helped resolve a debate. *Bull. Amer. Meteor. Soc.*, **99**, 837–839, <https://doi.org/10.1175/BAMS-D-17-0157.1>.
- Reynolds, C. A., and R. Gelaro, 2001: Remarks on Northern Hemisphere forecast error sensitivity from 1996 to 2000. *Mon. Wea. Rev.*, **129**, 2145–2153, [https://doi.org/10.1175/1520-0493\(2001\)129<2145:RONHFE>2.0.CO;2](https://doi.org/10.1175/1520-0493(2001)129<2145:RONHFE>2.0.CO;2).
- , —, and J. D. Doyle, 2001: Relationship between singular vectors and transient features in the background flow. *Quart. J. Roy. Meteor. Soc.*, **127**, 1731–1760, <https://doi.org/10.1002/qj.49712757514>.
- , J. D. Doyle, and X. Hong, 2016: Examining tropical cyclone–Kelvin wave interactions using adjoint diagnostics. *Mon. Wea. Rev.*, **144**, 4421–4439, <https://doi.org/10.1175/MWR-D-16-0174.1>.
- , —, F. M. Ralph, and R. Demirdjian, 2019: Adjoint sensitivity of North Pacific atmospheric river forecasts. *Mon. Wea. Rev.*, **147**, 1871–1897, <https://doi.org/10.1175/MWR-D-18-0347.1>.
- Rodwell, M. J., and Coauthors, 2013: Characteristics of occasional poor medium-range weather forecasts for Europe. *Bull. Amer. Meteor. Soc.*, **94**, 1393–1405, <https://doi.org/10.1175/BAMS-D-12-00099.1>.
- Rutledge, S. A., and P. V. Hobbs, 1983: The mesoscale and microscale structure of organization of clouds and precipitation in midlatitude cyclones. VIII: A model for the “seeder-feeder” process in warm-frontal rainbands. *J. Atmos. Sci.*, **40**, 1185–1206, [https://doi.org/10.1175/1520-0469\(1983\)040<1185:TMAMSA>2.0.CO;2](https://doi.org/10.1175/1520-0469(1983)040<1185:TMAMSA>2.0.CO;2).
- Schäfer, A. G., and F. Harnisch, 2015: Impact of the inflow moisture on the evolution of a warm conveyor belt. *Quart. J. Roy. Meteor. Soc.*, **141**, 299–310, <https://doi.org/10.1002/qj.2360>.
- , and Coauthors, 2018: The North Atlantic Waveguide and Downstream Impact Experiment. *Bull. Amer. Meteor. Soc.*, **99**, 1607–1637, <https://doi.org/10.1175/BAMS-D-17-0003.1>.
- Schwierz, C., S. Dirren, and H. C. Davies, 2004: Forced waves on a zonally aligned jet stream. *J. Atmos. Sci.*, **61**, 73–87, [https://doi.org/10.1175/1520-0469\(2004\)061<0073:FWOAZA>2.0.CO;2](https://doi.org/10.1175/1520-0469(2004)061<0073:FWOAZA>2.0.CO;2).
- Shutts, G. J., 1990: Dynamical aspects of the October storm, 1987: A study of a successful fine-mesh simulation. *Quart. J. Roy. Meteor. Soc.*, **116**, 1315–1347, <https://doi.org/10.1002/qj.49711649604>.
- Snyder, C., and R. S. Lindzen, 1991: Quasi-geostrophic Wave-CISK in an unbounded baroclinic shear. *J. Atmos. Sci.*, **48**, 76–86, [https://doi.org/10.1175/1520-0469\(1991\)048<0076:QGWICIA>2.0.CO;2](https://doi.org/10.1175/1520-0469(1991)048<0076:QGWICIA>2.0.CO;2).
- Stappers, R., and J. Barkmeijer, 2011: Properties of singular vectors using convective available potential energy as a final time norm. *Tellus*, **63**, 373–384, <https://doi.org/10.1111/j.1600-0870.2010.00501.x>.
- Szunyogh, I., Z. Toth, R. E. Morss, S. J. Majumdar, B. J. Etherton, and C. H. Bishop, 2000: The effect of targeted dropsonde observations during the 1999 Winter Storm Reconnaissance program. *Mon. Wea. Rev.*, **128**, 3520–3537, [https://doi.org/10.1175/1520-0493\(2000\)128<3520:TEOTDO>2.0.CO;2](https://doi.org/10.1175/1520-0493(2000)128<3520:TEOTDO>2.0.CO;2).
- Tan, Z.-M., F. Zhang, R. Rotunno, and C. Snyder, 2004: Mesoscale predictability of moist baroclinic waves: Experiments with parameterized convection. *J. Atmos. Sci.*, **61**, 1794–1804, [https://doi.org/10.1175/1520-0469\(2004\)061<1794:MPOMBW>2.0.CO;2](https://doi.org/10.1175/1520-0469(2004)061<1794:MPOMBW>2.0.CO;2).
- Thorpe, A. J., 2004: Weather forecasting: A centenary perspective. *Weather*, **59**, 332–335, <https://doi.org/10.1256/wea.87.04>.
- Torn, R. D., and G. J. Hakim, 2008: Ensemble-based sensitivity analysis. *Mon. Wea. Rev.*, **136**, 663–677, <https://doi.org/10.1175/2007MWR2132.1>.
- , and —, 2009: Initial condition sensitivity of western Pacific extratropical transitions determined using ensemble-based sensitivity analysis. *Mon. Wea. Rev.*, **137**, 3388–3406, <https://doi.org/10.1175/2009MWR2879.1>.
- Ulbrich, U., A. H. Fink, M. Klawa, and J. G. Pinto, 2001: Three extreme storms over Europe in December 1999. *Weather*, **56**, 70–80, <https://doi.org/10.1002/j.1477-8696.2001.tb06540.x>.
- Vukicevic, T., and R. M. Errico, 1993: Linearization and adjoint of parameterized moist diabatic process. *Tellus*, **45A**, 493–510, <https://doi.org/10.3402/tellusa.v45i5.15051>.
- Walser, A., M. Arpagaus, C. Appenzeller, and M. Leutbecher, 2006: The impact of moist singular vectors and horizontal resolution on short-range limited-area ensemble forecasts for two European winter storms. *Mon. Wea. Rev.*, **134**, 2877–2887, <https://doi.org/10.1175/MWR3210.1>.
- Wernli, H., and H. C. Davies, 1997: A Lagrangian-based analysis of extratropical cyclones. I. The method and some applications. *Quart. J. Roy. Meteor. Soc.*, **123**, 467–489, <https://doi.org/10.1002/qj.49712353811>.
- , S. Dirren, M. Liniger, and M. Zillig, 2002: Dynamical aspects of the life-cycle of the winter storm “Lothar” (24–26 December 1999). *Quart. J. Roy. Meteor. Soc.*, **128**, 405–430, <https://doi.org/10.1256/003590002321042036>.
- Zhang, F., C. Snyder, and R. Rotunno, 2002: Mesoscale predictability of the “surprise” snowstorm of 24–25 January 2000. *Mon. Wea. Rev.*, **130**, 1617–1632, [https://doi.org/10.1175/1520-0493\(2002\)130<1617:MPOTSS>2.0.CO;2](https://doi.org/10.1175/1520-0493(2002)130<1617:MPOTSS>2.0.CO;2).
- , —, and —, 2003: Effects of moist convection on mesoscale predictability. *J. Atmos. Sci.*, **60**, 1173–1185, [https://doi.org/10.1175/1520-0469\(2003\)060<1173:EOMCOM>2.0.CO;2](https://doi.org/10.1175/1520-0469(2003)060<1173:EOMCOM>2.0.CO;2).
- , N. Bei, R. Rotunno, C. Snyder, and C. C. Epifanio, 2007: Mesoscale predictability of moist baroclinic waves: Convection permitting experiments and multistage error growth dynamics. *J. Atmos. Sci.*, **64**, 3579–3594, <https://doi.org/10.1175/JAS4028.1>.
- Zhou, F., and X. Cui, 2015: The adjoint sensitivity of heavy rainfall to initial conditions in debris flow areas in China. *Atmos. Sci. Lett.*, **16**, 485–491, <https://doi.org/10.1002/asl.586>.
- Zhu, Y., and R. E. Newell, 1998: A proposed algorithm for moisture fluxes from atmospheric rivers. *Mon. Wea. Rev.*, **126**, 725–735, [https://doi.org/10.1175/1520-0493\(1998\)126<0725:APAFMF>2.0.CO;2](https://doi.org/10.1175/1520-0493(1998)126<0725:APAFMF>2.0.CO;2).
- Zou, X., I. M. Navon, and J. Sela, 1993: Control of gravitational oscillations in variational data assimilation. *Mon. Wea. Rev.*, **121**, 272–289, [https://doi.org/10.1175/1520-0493\(1993\)121<0272:COGOIV>2.0.CO;2](https://doi.org/10.1175/1520-0493(1993)121<0272:COGOIV>2.0.CO;2).